TÉCNICO LISBOA

Methodology Development for BEV HV-Battery Durability Analysis based on Vehicle Dynamics

Luís Miguel Ferreira Figueiredo

Thesis to obtain the Master of Science Degree in

Mechanical Engineering

Supervisors: Prof. Aurélio Lima Araújo
Prof. Luís Filipe Galrão dos Reis

Examination Committee

Chairperson: Prof. Paulo Rui Alves Fernandes
Supervisor: Prof. Aurélio Lima Araújo
Member of the Committee: Prof. Hugo Filipe Diniz Policarpo

November 2021

Dedicated to my parents, Donzília and Luís, and my brother Henrique

Acknowledgments

I would like to thank my family, friends, colleagues, and university professors who contributed to the success of my academic path and in particular of this dissertation.

Thanks to my university supervisors prof. Aurélio Araújo and prof. Luís Reis for the availability, assistance and valuable feedback, as well as the willingness to supervise this dissertation. Thanks to my colleagues from the DAD and DAM departments at AVL for the pertinent advices, feedback and support throughout my thesis. Especially, thanks to my AVL supervisor Mehdi Mehrgou, for giving me the chance of working in my thesis at AVL during such an uncertain period for the global industry, and also for the knowledge and guidance during the course of the thesis.

Thanks to my closest friends in Graz, Martin, Maria, Klara, Mirna, Kayo and Božidar for the trips around Austria, talks, laughs, hang-outs and other *amazing* moments that I will forever remember.

To my friends in Lisbon, Rodrigo, Camané, Vítor Hugo, Henrique, Barbão, Bibão and more for the company, support and joyfull meetings during my university times.

Last, but certainly not least, thanks to my mother and father for investing in my education, for believing in me and for the unconditional support given to me during my life. Thank you mom, for making sure that I was never alone in Austria, for putting so much effort in my progress and success and for giving me and Henrique a level of education that the entire family can be proud of.

Resumo

Esta tese foca-se no desenvolvimento de uma nova abordagem à simulação estrutural de baterias de alta tensão de automóveis 100% elétricos.

Atualmente, os fabricantes automóveis recorrem a *shakers* com o objetivo de testar as baterias dos automóveis. Este procedimento envolve fixar a bateria a uma estrutura mais rígida que a carroçaria do veículo à qual é aplicada uma vibração aproximadamente gaussiana que, consequentemente, faz vibrar a bateria. Num contexto de vida real, o carregamento sofrido pela bateria tem características diferentes, dado que a bateria apresenta deformações globais, como resultado da flexibilidade da carroçaria. Na prática, isto significa que o dano gerado na bateria durante o teste pode estar a ser subestimado em comparação com o dano real.

O modelo de corpos múltiplos do Audi E-Tron é submetido a simulações dinâmicas onde o automóvel se desloca em estradas com diferentes irregularidades, representativas de uma situação de vida real. Numa outra vertente, é feita uma simulação dinâmica da bateria no *shaker test* de onde se obtêm acelerações em pontos específicos. Estas acelerações são validadas com medidas experimentais e consideradas no cálculo do pseudo-dano com recurso ao método de contagem *rainflow*. As acelerações do *shaker test* e das simulações ao nível do veículo são comparadas em termos de PSD (Densidade de Potência Espectral) e pseudo-dano, concluindo-se que as simulações ao nível do veículo contribuem até 80 vezes mais para o dano da bateria, indicando que o método mais apropriado para avaliar a durabilidade da bateria é a simulação ao nível do veículo.

Abstract

This thesis focuses on the development of a new approach to the structural simulation of high voltage batteries of BEVs (Battery Electric Vehicles).

Currently, car manufacturers resort to shakers for the purpose of testing car batteries. This procedure involves attaching the battery to a very rigid structure to which an approximately gaussian vibration signal is applied, therefore vibrating the battery. In a real-life context, the loading suffered by the battery has different characteristics, given that the battery has global deformations as a result of the flexibility of the bodywork. In practice, this means that the damage generated to the battery during the test may be underestimated compared to the actual damage.

In this thesis, the multi-body model of the Audi E-Tron is subjected to dynamic simulations where the car travels on road profiles with different irregularities, representative of the roads in a real-life situation. In another strand, a dynamic simulation of the battery is made in a *shaker test* from which accelerations are obtained at specific points. These accelerations are validated with experimental measures and considered in the calculation of pseudo-damage using the rainflow counting method. The accelerations of the shaker test and vehicle-level simulations are compared in terms of PSD (Power Spectral Density) and pseudo-damage, concluding that vehicle-level simulations contribute up to 80 times more to the battery pseudo-damage, indicating that this is the most appropriate mean of evaluating the durability of the battery.

Contents

List of Tables

List of Figures

Nomenclature

Greek symbols

α, β Basquin curve parameters.

Δ Range.

γ_2 Kurtosis coefficient.

λ Wavelength.

Ω Spatial frequency.

ω Angular frequency.

ϕ Mode shape vector.

Roman symbols

d Pseudo-damage.

F Force.

f Frequency.

G_d Displacement PSD of roughness-characterised roads.

J Torsional moment of inertia.

K Stiffness matrix.

M Mass matrix.

N Number of constant amplitude load cycles.

S Stress amplitude.

t Time.

u Displacement vector.

y Modal participation factor.

Subscripts

A 1st MAC correlation dataset.

i Mode number in modal superposition.

m Master node.

q 2nd dataset mode number.

r 1st dataset mode number.

s Slave node.

sim Simulation.

X 2nd MAC correlation dataset.

Superscripts

T   Transpose.

Glossary

ARB Anti-Roll Bar.

BEV Battery Electric Vehicle.

BiW Body in White.

CF Crest Factor.

DOE Design Of Experiments.

DOF Degree Of Freedom.

DUT Device Under Testing.

EU European Union.

FRF Frequency Response Function.

HV High-Voltage.

IEC International Electrotechnical Commission.

MAC Modal Assurance Criterion.

MAST Multi-Axial Shaker Testing.

MBS Multibody Simulation.

MPF Modal Participation Factor.

NVH Noise, Vibration, Harshness.

OEM Original Equipment Manufacturer.

PDF Power Density Function.

PSD Power Spectral Density.

RMS Root-Mean Square.

SoC State of Charge.

SUV Sports Utility Vehicle.

14

Chapter 1

Introduction

1.1 Motivation

Electric and hybrid vehicles have been pointed by the European Union as important tools to decrease the emissions of greenhouse gases. As of 2019, 30% of the total CO_2 emissions in the EU were provenient from transportation, of which 72% correspond to road transportation emissions, making it the largest contributor towards global warming [1]. Within the scope of the Green Deal, the European Commission has proposed a decrease of 55% in the emission of greenhouse effect gases comparing to the levels of 1990, surpassing the already existing target of 40% [2]. Furthermore, the recently established goal for car makers in 2020/21 sets a maximum fleet-wide average emission of 95 g CO_2/Km, further pressuring automotive manufacturers to change the type of powertrain used from full internal combustion to electric and hybrid models [3]. In fact, some countries and states have already announced future bans on the sale of gasoline and diesel-powered cars [4].

Due to these new regulations and customer demand as well, the automotive industry is undergoing a shift towards the implementation of electric powertrains in automobiles [5].

Additionally, automotive manufacturers are obligated to design vehicles that can operate safely under regular and predicted events that take place during the working life of the vehicle [6]. It is crucial that the durability assessment of these components is carried out during the early-stages of design, so that critical components or areas are targeted and their design can be changed. Proceeding to such alterations later in the development stage can be costly and time-consuming [7].

In the specific case of electric vehicles, it is important to ensure the durability requirements of novel components, such as the High-Voltage Battery (HV Battery), are met. More specifically, Battery Electrical Vechicles (BEV's) have large batteries that account for one third of the vehicle's entire weight [6].

Due to their size, HV batteries now affect the dynamics of the chassis structure due to the coupling effect between both structures (battery and chassis). This means that large battery systems now undergo global deformations as they deform together with the flexible structure that supports them [6].

Furthermore, in a real-life scenario, these batteries are subjected to non-gaussian dynamic excitations in the time domain, that, despite of being more damaging, can have the same Power Spectral

Density (PSD) profile in the frequency domain as the gaussian signal [8]. Gaussian time signals have a PDF (Probability Density Function) for every instant of time that can be fully characterized by its mean value (μ) and variance (σ^2). However, the PDF of the non-gaussian signals depends on additional parameters to be fully determined. Two of the parameters of interest analysed in this disseration are the crest factor (CF) and the kurtosis coefficient (γ_2). The IEC 60068-2-64:2008 [9] standard states that, in a shaker test, the frequency-to-time-domain conversion of the excitation has to result in an approximately gaussian time signal.

The current testing procedures for large BEV batteries resort to shaker tests, in which stiff jigs are used to fix the battery whilst shaking the jig with a random gaussian time signal extracted from standardized PSD profiles. However, this procedure does not consider the flexible battery attachments of the battery. This means that global deformations in the battery are disregarded during this test, and, given the flexibility of the BiW (Body in White) that supports the battery, this means disregarding a fundamental characteristic of life-representative testing [6].

Additionally, non-gaussian leptokurtic excitations (positive γ_2) have shown to bring an additional damage contribution to the DUT (Device Under Testing) [8]. By applying a gaussian excitation to the HV battery in a shaker test, that additional damage contribution is also not being considered. Since both the gaussian and non-gaussian signals have the same PSD in the frequency domain [8], an effective damage assessment can be better performed in the time domain instead.

This dissertation focuses in developing a new method for the structural simulation of a BEV HV-Battery in the time domain and considering its flexible attachments. It is important to understand if the current procedures for BEV HV-battery vibration testing underestimate the damage that is generated. Therefore, the battery is integrated in a simplified model of the BiW and full-vehicle simulations are performed. This simplified model (hereinafter referred to as "beams model") consists of a frame structure composed by beam elements that has a similar dynamic behaviour as the BiW. This model is built based on the amount of information available about the BiW in very early stages of vehicle design, when detailed information about the overall BiW is scarce, and only the global stiffness and mass properties are known.

These vehicle simulations are performed using 5 different uneven road profiles. In parallel with this simulation loop, a digital twin of the shaker test is created (shaker simulation). To validate the shaker simulation results, experimental acceleration measurements are obtained from specific points in the battery. A repetition quantity for each simulation and test type is calculated so that the damage comparison can be done for the same level of vehicle usage in all different simulations and test. Finally, the acceleration measurements from the vehicle simulations, battery shaker simulation and shaker test are compared in terms of their PSD, and a pseudo-damage parameter will be calculated for each of them. The pseudo-damage generated in all different situations is compared in order to identify the most damaging scenario.

1.2 Topic Overview

The following topics require special comprehension, as they serve as the starting point for this dissertation:

- **External excitation load** : Dynamic loads are applied to the battery during the shaker test and to the car in the entire-vehicle analyses. These loads are responsible for the excitation of the structure's eigenmodes.

- **Shaker vibration test** : The battery is fixed to the shaker test-bed and is shaken vertically with an acceleration time signal derived from a PSD (Power Spectral Density) profile. This testing prodedure is widely used in the electric automotive industry.

- **Modal superposition** : This method allows the calculation of the deformation of a structure as a linear combination of some of its natural mode shapes.

- **Pseudo-damage** : Allows a damage comparison to be done based on the severity of measured signals (can be displacements, velocities, accelerations or forces). This approach does not account for material properties.

1.3 Objectives

This dissertation aims at proposing a new HV-battery simulation methodology for durability analysis focused on BEV's as a solution to tackle the current limitations of the standard procedures used in the automotive industry. This will be achieved by means of full-vehicle simulations with an included battery model.

Additionally, to tackle the excess of detailed information in the BiW model, a similar beams model is created. The beams model has similar modal properties as the BiW model whilst having a much lower numerical complexity, and is replaced by the detailed BiW model in the full-vehicle multibody dynamic simulations. The beams model aims to replicate the level of BiW information available at very early stages of vehicle development.

It is also the aim of this dissertation to compare the results from all dynamic loadings (battery shaker simulation, battery shaker test and vehicle simulations) and compare the overall modal participation in both scenarios.

From the dynamic simulations and shaker test, the acceleration at 4 different locations is intended to be measured. These acceleration time signals are then compared by means of their PSD profiles.

Finally, it is necessary to calculate the pseudo-damage from the acceleration time signals obtained in the simulations and test. In a solely comparative way, this parameter will be useful in identifying significant differences between the considered loadings.

1.4 Dissertation Outline

This dissertation is divided in the following chapters:

- **Background** : Theoretical principles that serve as a base for the model construction and numerical calculations done in this work. Other state-of-the-art topics relative to HV-battery testing are also addressed.

- **HV-Battery model** : The models used in this dissertation can be split in two large groups: the battery and the full-vehicle models. This section describes the construction of the battery model for the shaker simulation and vehicle integration.

- **Full-vehicle models** : Description of the different types of chassis considered in the vehicle assembly as well as the suspension model.

- **Design of Experiments** : Detailed description of the simulation setup for both the HV-battery and the vehicle simulations.

- **Results** : Presentation of the modal participation factors for each of the simulations, calculation of the number of repetitions for each vehicle simulation, comparison of the PSD's for the simulated and experimental acceleration time signals and calculation of the pseudo-damage parameter.

1.5 Thesis Context

This dissertation was developed in collaboration with AVL List GmbH (*Anstalt für Verbrennungskraftmaschinen List*), located in Graz, Austria. Over the course of 6 months, most of the literature study, software learning, modelling and simulations were done in the company's facilities.

AVL is an automotive consultancy company that develops projects in a broad variety of areas of the sector. Every year, the company offers several dissertation positions in these areas. This thesis was developed in the NVH (Noise, Vibration, Harshness) and Multibody Simulation team of the DAD department.

Chapter 2

Background

This section of the thesis focuses on providing the theoretical insights that will enable the understanding of the remaining sections.

2.1 Dynamic Analysis

The governing equations for a dynamic analysis can be deduced from the d'Alembert Principle, the Virtual Work Method or the Hamilton's principle are written in the following form [10]:

$$[M]\{\ddot{u}\} + [C]\{\dot{u}\} + [K]\{u\} = \{f\}(t) \tag{2.1}$$

Where $[M]$, $[C]$ and $[K]$ are the global mass, damping and stiffness matrices respectively; $\{u\}$, $\{\dot{u}\}$ and $\{\ddot{u}\}$ are the displacement, velocity and acceleration vectors respectively.

2.1.1 Modal Analysis

The modal analysis is a particular kind of a dynamic analysis that applies to the study of the behaviour of a structure under free-vibrations, meaning that, for this case, the external forces applied in the structure are null. In some studies, damping models are included in the modal analysis formulation to estimate a damped system response [11]. However, it is a common practise in engineering to study the undamped system response of structural models, as it simplifies the formulation of the dynamic analysis problem and provides an insight to the damped response [12]; for these reasons, the damping effects will be neglected in this analysis. Therefore, the resulting system of equation is the following [13]:

$$[M]\{\ddot{u}\} + [K]\{u\} = \{0\} \tag{2.2}$$

The solution of this equation is a sinusoidal function:

$$\{u\} = \{\phi\}sin(\omega t) \tag{2.3}$$

Where ϕ and ω are the phase and angular frequency, respectively. By replacing the result of equation

5

2.3 in equation 2.2, the following equation is obtained:

$$([M]\omega^2 - [K])\{\phi\} = \{0\} \tag{2.4}$$

Equation 2.4 presents an eigenvalue problem. The eigenvalues obtained from the solution of this problem are the squares of the natural frequencies. The eigenvectors correspond to the mode shape vectors.

2.1.2 Guyan Reduction

The Guyan Reduction method, also known as static condensation, is a techique used to decrease the computational effort of a dynamic analysis whilst maintaining its accuracy. This method aims at reducing the complexity of the dynamic analysis equation by reducing the number of degrees of freedom (DOFs) involved in the equation. Only the DOF's of loaded nodes (i.e. the nodes that correspond to contact points of the component) are considered in the reduced equation [14].

This method is based on a re-organization of the static equilibrium equation, separating the DOFs of the master nodes (loaded nodes, denoted by "m") and the slave nodes (unloaded nodes, denoted by "s") as follows.

$$\begin{bmatrix} [K_{mm}][K_{ms}] \\ [K_{sm}][K_{ss}] \end{bmatrix} \begin{Bmatrix} u_m \\ u_s \end{Bmatrix} = \begin{Bmatrix} f_m \\ \{0\} \end{Bmatrix} \tag{2.5}$$

The second equation of the previous system of equations results in the following equation:

$$([K_{mm}]) = -[K_{ss}]^{-1}[K_{sm}]\{u_m\} \tag{2.6}$$

Replacing the result from equation 2.6 in the first equation of the matrix system 2.5 results in:

$$([K_{mm}] - [K_{ms}][K_{ss}]^{-1}[K_{sm}])\{u_m\} = \{f\} \tag{2.7}$$

Solving equation 2.7 requires only the determination of the DOF's associated with the master nodes, therefore reducing the computational effort of the analysis.

2.1.3 Modal Superposition

The modal superposition method suggests that the deformation of a body during a dynamic analysis can be given as a linear combination of the eigenmodes of that body, as follows:

$$\{u\} = \sum_i y_i \phi_i \tag{2.8}$$

Where ϕ_i is the ith mode shape and y_i is the Modal Participation Factor (MPF) of mode i for every instant of the simulation. During the dynamic simulation, the MPF's are calculated and output for every step of the simulation.

2.2 Coupling effect

The coupling effect consists in the modification of the modal properties of a structure due to added boundary conditions. Namely, the natural frequencies suffer noticeable increases and the mode shapes re-adapt to the imposed conditions. A simple demonstration of this effect was done in [15], where different boundary conditions were applied to a beam component of a building to reduce the seismic response. It was noticed that, with an increase of the number of constrained degrees of freedom in the tips of the beam, the frequencies become higher because the stiffness increases.

The boundary conditions applied to the component of interest may also consist of connections between the component of interest and surrounding parts. In this dissertation, this concept applies to the interaction between the battery and the chassis in the full-vehicle simulations.

2.3 Modal Assurance Criterion

The Modal Assurance Criterion (MAC) is used to correlate the mode shapes of two similar structures by associating the displacements (DOF's 1,2 and 3) of two comparable sets of nodes in the structure. The MAC value is a number between 0 and 1. The closer this value is to 1, the better the correlation is, i.e. the more similar the mode shapes are.

The MAC is defined as the normalized product of two modal vectors from different datasets (A and X), mode r is compared with mode q. A and X can contain only the displacement in specific nodes that are relevant for the correlation. Figure 2.1 displays an overlayed image of the two structures from which the MAC will be calculated. The nodes that were considered for the MAC correlation are highlighted in the figure. Notice that the node density is higher in the battery area (chassis floor), which is the area of interest. The MAC value is given by:

$$MAC = \frac{|\{\phi_A\}_r^T\{\phi_A\}_q|^2}{(\{\phi_A\}_r^T\{\phi_A\}_r)(\{\phi_X\}_q^T\{\phi_X\}_q)} \tag{2.9}$$
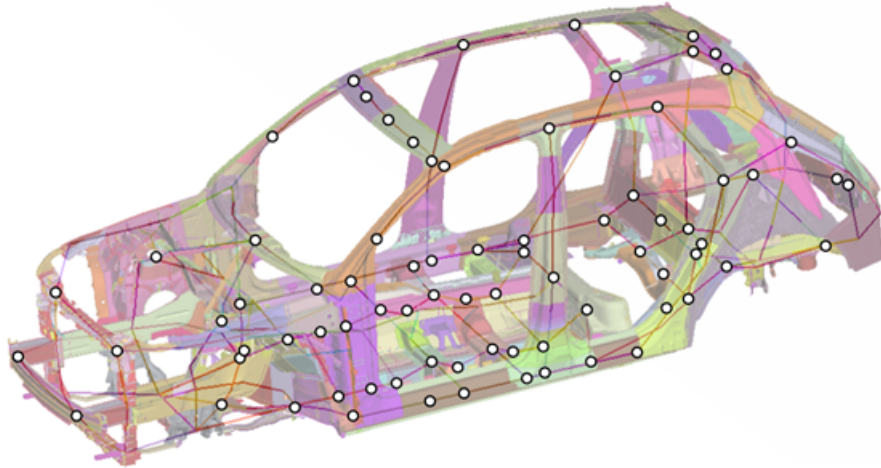
Figure 2.1: Nodes used in the MAC correlation

2.4 BEV HV-Battery mechanical testing

This section focuses only on two tests that are considered to be the most relevant for this dissertation: the hammer test and the shaker test. Some authors approach other mechanical vibration tests for HV-Batteries, such as the MAST (Multi-Axial Shaker Test) and the 4-post test. The 4-post-test consists of a full-vehicle test in which a vertical excitation load is applied to each wheel individually. Dörnhöfer [6] points out this test as an alternative to tackle the limitations of battery-level testing. The MAST test was used by some authors to evaluate electrical properties and the natural frequencies of the battery cells [16].

However, none of the aforementioned tests is widely used in the automotive industry, being the shaker test the most preferred by OEM's when it comes to HV-Battery vibration testing. The shaker test is described in the sub-section 2.4.2.

2.4.1 Hammer test

From the constructor's point of view, it is important to compare the results of the modal analysis with practical measurements that can enable the validation of the natural frequencies and mode shapes. A mismatch between the measured results and the computational ones may indicate the presence of unaccounted defects in the HV battery.

The hammer test allows the experimental determination of the vibration frequencies and mode shapes via short-duration impact loading. The hammer is equiped with a load cell that generates a time signal of the impact force [17]. Besides that, 29 tri-axial accelerometers were placed in the battery in the locations shown in figure 2.2. FRF (Frequency Response Function) are calculated from the accelerometer measurements, allowing the identification of the most predominant mode shapes and the respective vibration frequencies [18][19].
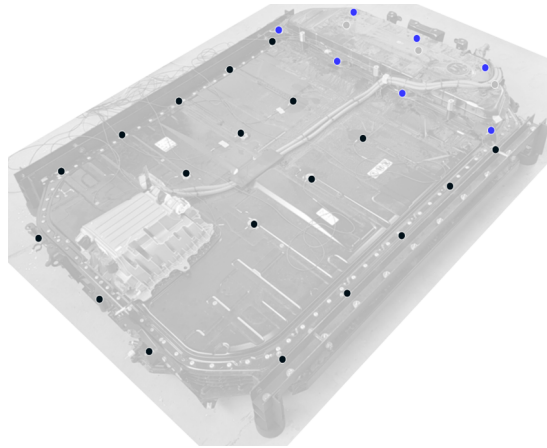
Figure 2.2: Location of the tri-axial accelerometers in the battery pack for the hammer test

2.4.2 Shaker test

Currently, shaker vibration testing is the most common procedure of HV battery mechanical testing. Most commonly, an electrodynamic shaker is used to apply two distinct excitations: sine-sweep (sine wave excitation load with a time-increasing frequency); or a white noise excitation (random vibration) that can have a frequency band upper limit of more than 2 KHz [20]. This dissertation will focus on the latter. Figure 2.3 shows the setup for the shaker test.
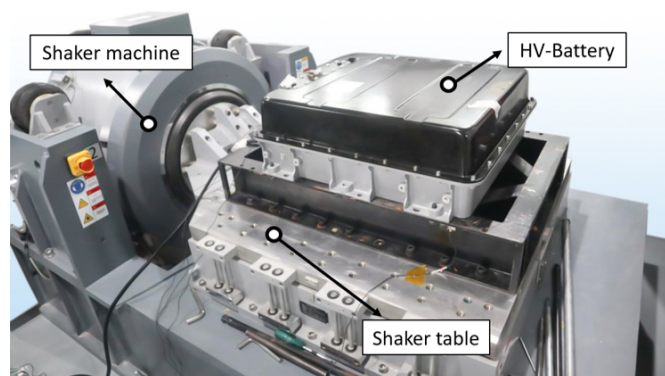
Figure 2.3: Setup for the shaker test [21]

During a shaker test with a random excitation, the DUT (Device Under Testing) undergoes a vertical excitation given by a time signal that is derived from a PSD profile, addressed in section 2.5. According to some of the available standards for shaker vibration testing of H batteries([22][23]), it is not a regular procedure to carry a vibration test without performing ambient temperature and charging/discharging cycles simultaneously. However, the thermal and charging cycles are not approached in this project.

2.5 PSD profile

PSD profiles are widely used in automotive engineering applications to characterise random vibration signals. This method consists of a normalization of the Fast Fourier Transform (FFT) of a random time

signal to the frequency sampling rate, so that the dependency of the duration of the signal is lost. That way, PSD's derived from signals that have different time lengths can be compared whilst using a smaller amount of data [24].

To obtain a PSD, the time signal must be first divided into stretches. In the neighbourhood of each dividing line, discontinuities may occur. These discontinuities influence the PSD with an artificial very high frequency contribution that spoils the PSD measurement [25]. This is commonly known as the *leakage effect*, and to correct it, a windowing function such as the Hanning window function can be used [26]. This function is null in the neighbourhood of the dividing lines and 1 in the middle of the time stretch, as shown in figure 2.4.
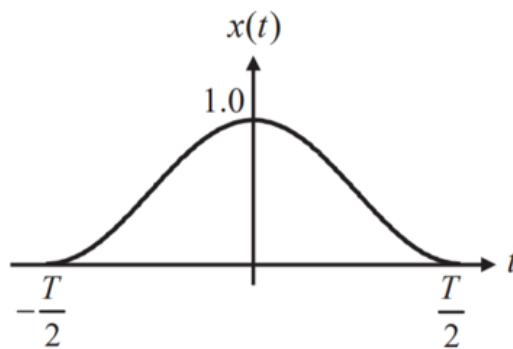
Figure 2.4: Hanning windowing function for a time stretch of length T

Multiplying each stretch of the time signal by its own Hanning window has previously shown to improve the accuracy of the PSD's frequency content [25]. Next, a FFT is calculated individually for each time stretch. Then, an average of all the squared FFT's is calculated and the resultant is divided by the sampling frequency rate in order to obtain the PSD profile. This process is schmatically represented in figure 2.5.
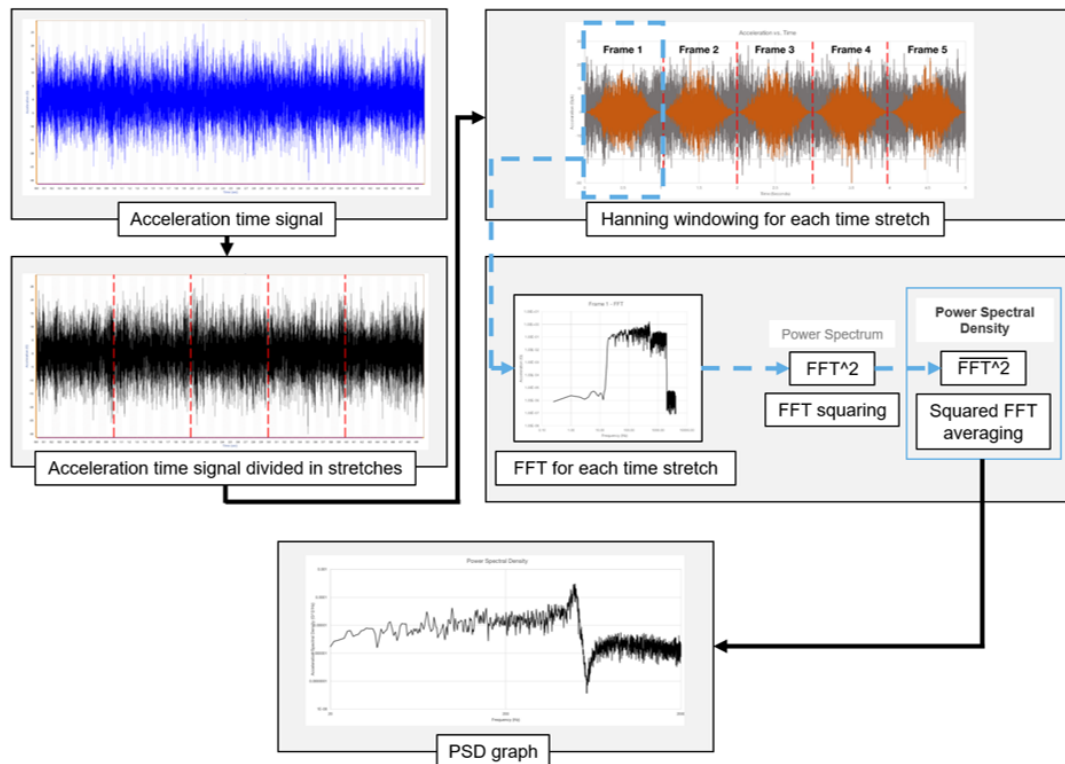
Figure 2.5: Schematic representation of the time-signal-to-PSD conversion process (images obtained from [27])

2.5.1 Standards of PSD profiles for HV-Battery vibration testing

Currently, there is a large variety of standards available for BEV HV-battery vibration testing. In these standards, the excitation load is not given in the time domain. Instead, the signals are provided in terms of their PSD due to the advantages mentioned before. Two of the available ISO standards for the purpose of HV-Battery testing are ISO 12405-1:2011 [22] and ISO 6469-1:2019 [23]. In both of these standards, it is defined that ambient temperature and SoC (State of Charge) cycles must be performed simultaneously with the vibration excitation. The duration of the vibration test according to ISO 12405-1 is 21h for spatial direction if only one sample is available. For ISO 6469-1, the test duration is 12h per spatial direction. The most prominent failure modes of a HV battery subjected to a vibration test carried out in accordance with these standards are the electrical contact loosening and material breakage.

Unlike the previous standards, the SAE standard J2380 vibration test [28] aims at reproducing the amount of damage in the HV battery correspondent to well-defined amount of vehicle usage, other than provoking certain modes of failure [29]. The amount of vehicle usage that corresponds to the damage generated by this standard is 100 000 miles (160 934 Km). In this standard, simultaneously with the vibration test, a SoC cycle is performed. The PSD profile for the SAE J2380 standard can be seen in figure 2.7.

In this dissertation, only the ISO 12405-1 standard will be analysed, since it is one of the most common standards in the automotive industry for HV-Battery vibration testing, highly requested by OEM's.

11

Additionally, the goal of this dissertation is to compare the standard loading to a vehicle-specific loading, and for that, it is more coherent to select a well-known, widely used standard.

Figure 2.6 presents the PSD profiles for the two aforementioned ISO standards. From this figure, it is possible to see that the PSD profiles were generally lowered from ISO 12405-1 to ISO 6469-1, suggesting that the damage generated by previous one will be comparatively larger. Moreover, the duration of the ISO 12405-1 test is twice as large as the one from IS0 6469-1, worsening the damage generated in the HV battery.

(a) ISO 12405-1 [22]   (b) ISO 6469-1 [23]
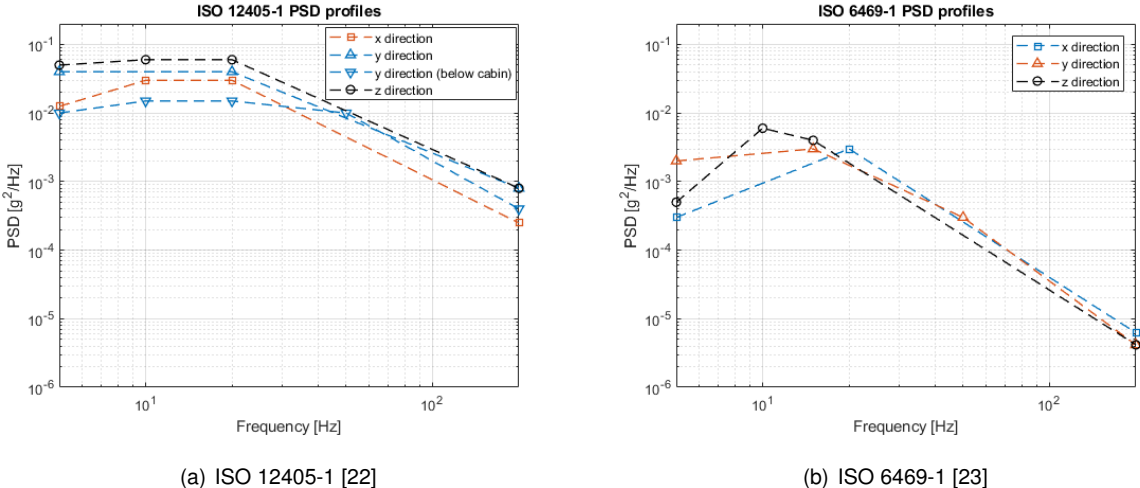
Figure 2.6: PSD profiles from two different ISO standards
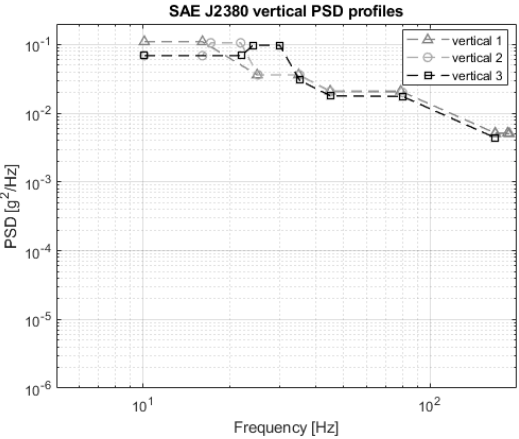
Figure 2.7: Vertical acceleration PSD profiles from standard SAE J2380

2.6   Statistical parameters of random time signals

To begin this section, it is useful to make a distinction between the various types of signals, presented graphically in figure 2.8 [26]. First, a distinction between deterministic and random time signals is made. In the random signal category, the stationary time signals are of particular interest. These time signals are characterised by having a probability density function (PDF) that does not change with time [30].
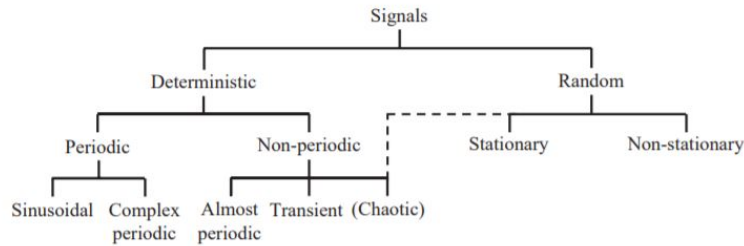
Figure 2.8: Schematic classification of time signals [31]

2.6.1 Gaussian time signals

The Gaussian signals are a particular case of the stationary random vibration signals, in which the PDF around the mean value is characterised by a gaussian distribution profile. These signals can be fully characterised by their mean value (μ) and the variance (σ^2). ISO 12405-1 specifies that the frequency-to-time-domain conversion of the dynamic excitation load must be carried according to the IEC 60068-2-64:2008 standard. This standard states that the time signal of the dynamic excitation must present an approximated gaussian distribution (see figure 2.9). However, experimentally measured random vibrations can have non-gaussian characteristics that increase the load severity. To characterise these signals, it is often needed to specify additional parameters described by Shin and Hammond [26] as *higher moments*. In particular, this diissertation focuses on the fourth moment, also known as the kurtosis coefficient (γ_2). Additionally, special attention will also be given to the crest factor. These parameters are addressed in section 2.6.2.

2.6.2 Non-Gaussian time signals

The following parameters are often used in engineering applications to characterise the severity of random excitation loads defined by non-gaussian time signals.

- **Kurtosis coefficient (γ_2)** : This parameter evaluates the flattening of the PDF of a certain signal around its mean value and it is given by equation 2.10, where E denotes the expected value and X is a sampled value of the signal. Gaussian signals have a null kurtosis coefficient. If the kurtosis is negative, the signal is known as platykurtic and the PDF becomes flatter. On the other hand, if the kurtosis is positive, the signal becomes leptokurtic and the PDF presents a peak around the mean value, meaning that this signal will have a higher amount load cycle peaks around the mean value (see "Zone 2" in figure 2.9). This will lead to a slight additional damage contribution. A side-effect from this concentration around the mean value is the raise of the PDF around its extremities (see zones 1 and 3 in figure 2.9). This means that a leptokurtic signal will have load cycles with a higher amplitude, bringing a much larger contribution to the pseudo-damage generated by this loading. In fact, Rissoan [8] concludes that most road excitation signals are of the Leptokurtic type, and that this type of loading can be up to 100 times more damaging than a gaussian signal.

$$\gamma_2 = \frac{E[X - \mu]^4}{\sigma^4} - 3 \tag{2.10}$$

- **Crest Factor** : This factor is a ratio between the maximum absolute value of a signal and its root-mean-square (RMS) value, given by expression 2.11. This factor is not bounded in a gaussian signal, there is no limit on how large the values on a signal of this nature can be. However, it is a quantification of the most damaging load cycle present in a signal (largest amplitude cycle), therefore, it becomes relevant from the load analysis point of view.

$$CF = \frac{X_{peak}}{X_{RMS}} = \frac{\max(|X|)}{\sqrt{\{X\}^2}} \tag{2.11}$$
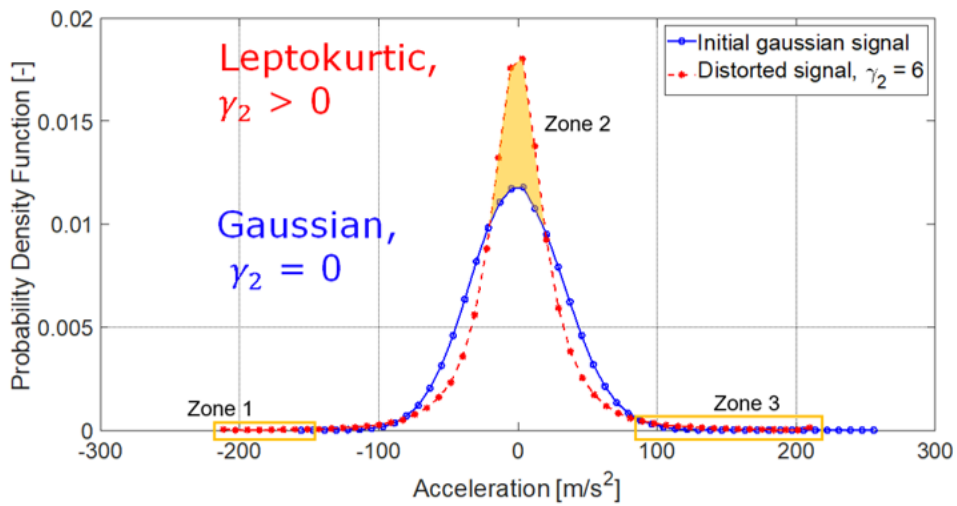
Figure 2.9: Gaussian and Leptokurtic distribution. The orange-signaled areas between the Gaussian and Leptokurtic profiles contribute to the severity of the leptokurtic loading. [8]

2.7 Rainflow counting method

The rainflow counting method has the objective of transforming complex stress time signals into well-characterised fatigue cycles. The rainflow counting method is hereby described in accordance to [32].

The first step for the application of the rainflow method is the determination of the stress time history. The Von-Mises stress distribution as a function of time can be determined using the modal superposition method, as it was done in [33]. From the time-varying stress distribution, the stress time history for specific points of interest can be determined. Figure 2.10 shows a generic stress time history. For the application of the rainflow counting method, it is often useful to rotate the stress-time diagram 90º for visualization purposes, as shown in figure 2.10 b).
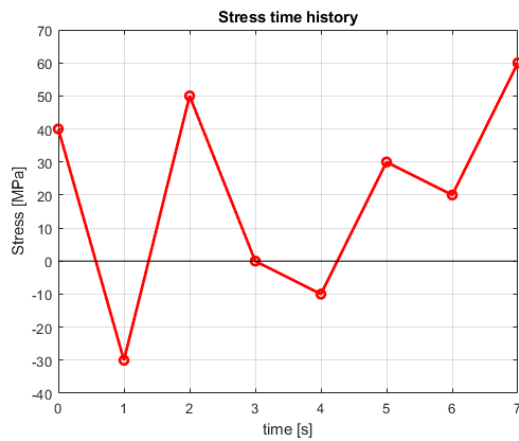
(a) Original   (b) Rotated 90º
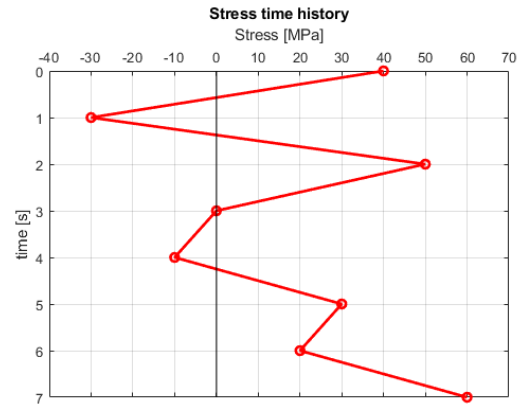
Figure 2.10: Stress time history - generic example

In a second stage, an analogy to a raindrop path across the entire vertical stress history graph is made, hence the name rainflow. All the rainflow paths are shown in figure 2.11.

The first rainflow path starts in point A and drops "to the ground" after passing by point B.

The next rainflow path starts in point B (where the previous path ended its contact with the stress-time diagram), passes by point C and drops until it meets the diagram stretch that leads it to point H, where it drops, once again, "to the ground", and the procedure repeats systematically.

The rainflow paths described in the previous two paragraphs correspond to the load cycles given by the points where they pass, i.e., cycles AB and BCH respectively.

In some cases, the rainflow path does not reach the ground. Instead, it meets a previously existing rainflow and stops there. In these cases, the last letter of the cycle is the last point where the previously existing cycle passes and a " ' " is put after the last letter (see the case of cycle EFC' in figure 2.11 and table 2.1 for instance).

Each of the rainflow paths of figure 2.11 corresponds to a load cycle. Table 2.1 presents the maximum, minimum and range values for every load cycle. The range (last column of table 2.1) is of special interest for the pseudo-damage calculations, as it corresponds to the double of the amplitude of a cycle.
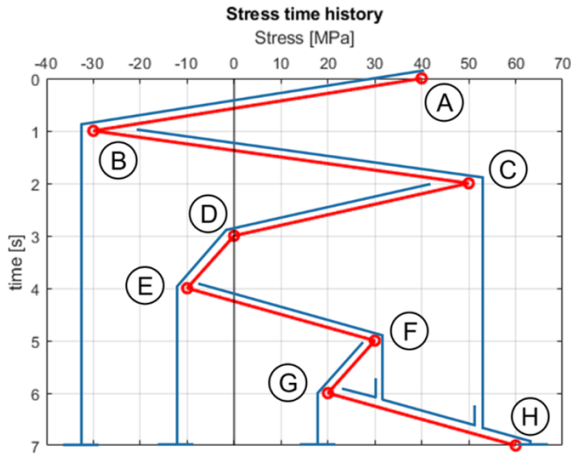
Figure 2.11: Rainflow paths

Table 2.1: Load cycle characteristics

Cycles	Lowest σ value [MPa]	Highest σ value [MPa]	Range [MPa]
AB	-30	40	70
BCH	-30	60	90
CDE	-10	50	60
EFC'	-10	50	60
FG	20	30	10
GF'	20	30	10

2.8 Pseudo-Damage

The fatigue analyses that are generally used to calculate the damage on structures are costly, as they process (and post-process) a large amount of data to generate damage and durability results. Therefore, a simpler way of estimating the damage on a structure undergoing a dynamic loading is needed.

As a solution to this issue, in this dissertation, the pseudo-damage concept is used as a comparative measure of load severity between two different types of loadings. The psedo-damage concept was already used in previous studies. Lévai [34] resorts to the pseudo-damage concept to compare different loading scenarios on a BiW without accounting for material properties. The acceleration was obtained in 34 different locations in 3 DOF's. The pseudo-damage was then calculated for each acceleration signal in order to determine which of the 72 signals better describes the actual damage of the structure. Prakash [35] uses frequency-domain measuring techniques to obtain acceleration time signals from which the pseudo-damage is calculated. This method is then compared to a strain-based fatigue calculation approach. In both of these studies, the pseudo-damage was calculated from measured acceleration time signals, without the influence of material properties, with the objective of reducing the amount of data to process.

The basis for the definition of the pseudo-damage concept is the Basquin S-N curve definition [31]. Originally, this method is only applicable for fully reversed stress time signals, i.e., signals whose mean value is zero and that have a constant stress amplitude [36]. However, Johannesson and Speckert [31] suggest this procedure can be modified to analyse a broader variety of time signals that do not necessarily need to be stress histories nor be fully reversed signals. The Basquin equation is given by:

$$S = \alpha N^{-\beta} \tag{2.12}$$

Where S denotes stress amplitude, N is the number of cycles carried at a constant stress amplitude

until failure, and α and β are material-dependent parameters determined experimentally. The damage contribution for one single cycle with a constant amplitude is given according to the Palmgren-Miner rule [31]:

$$D = \sum_i \frac{1}{N} = \frac{1}{\alpha} \sum_i \frac{1}{S_i^{-\beta}} \tag{2.13}$$

Where i denotes the number of the constant amplitude cycle considered. The goal is that the pseudo-damage definition is dependent on the least possible amount of material paramters. For that reason, and for comparative purposes, the α constant is left out of the pseudo-damage calculation, meaning that the pseudo-damage is given by:

$$d = \sum_i S_i^{\beta} \tag{2.14}$$

The cycle characteristics can be obtained from the cycle counting methods available in [31]. However, this thesis will only focus in the rainflow counting method, described in greater detail in the previous subsection. The pseudo-damage approach is less accurate in signaling critical areas of interest for fatigue investigation but is more time-efficient and allows one to detect large differences in the severity of the dynamic loading. The pseudo-damage concept can be applied to any time signal (displacement, velocity, acceleration or force) [26].

2.9 Workflow

The following image briefly explains the workflow that was followed throughout the course of this thesis. The MAC correlation phase involves an iterative process of improvement of the beams model.
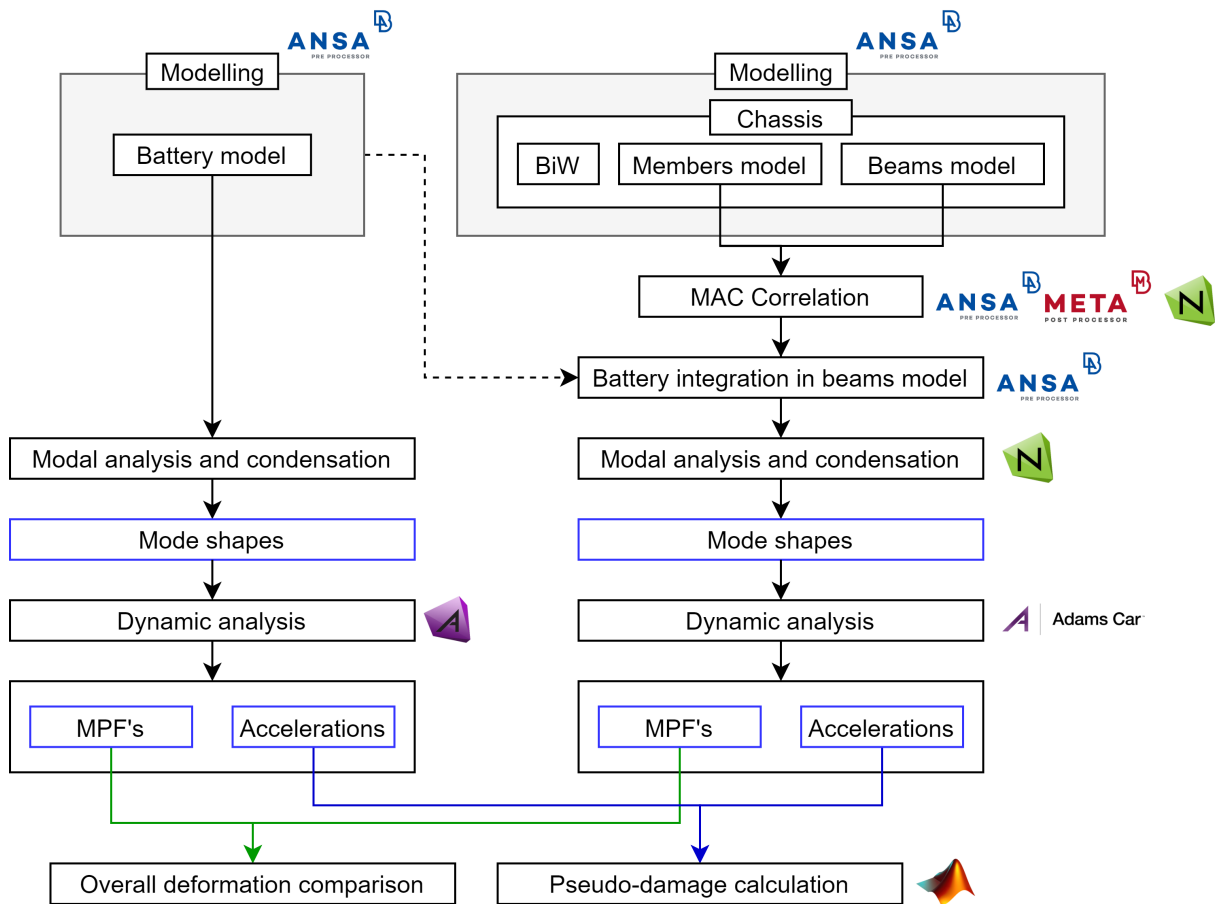
Figure 2.12: Schematic dissertation workflow

Chapter 3

HV-Battery model

This chapter is dedicated to the explanation of the High Voltage Battery (HV Battery) model, its components, and modelling considerations. Later in this section, the battery finite element model is compared to the actual HV-Battery in terms of mass and modes of vibration.

3.1 Overall features

The vehicle model considered for this thesis is the Audi E-tron 55 Quattro Edition One 2019. This is the first fully electric SUV produced by Audi. Battery Electric Vehicles (BEV) like this one feature large batteries that usually weigh more than 600 Kg, roughly one third of the car's weight [6].

This particular battery has the capability of storing 95 KWh of energy, nominal voltage of 396 V, its own fluid-cooling circuit [37] and the dimensions indicated in the figure 3.1. Each cell module includes 12 cells. The battery has 36 cell modules contained inside two compartiments: the main compartiment (31 cell modules) and the top compartiment (5 cell modules). The battery also features a crash structure of its own in the main compartiment. Figure 3.2 provides an exploded view with the most relevant components of the battery.

<div align="center">

(a) Side view   (b) Rear View
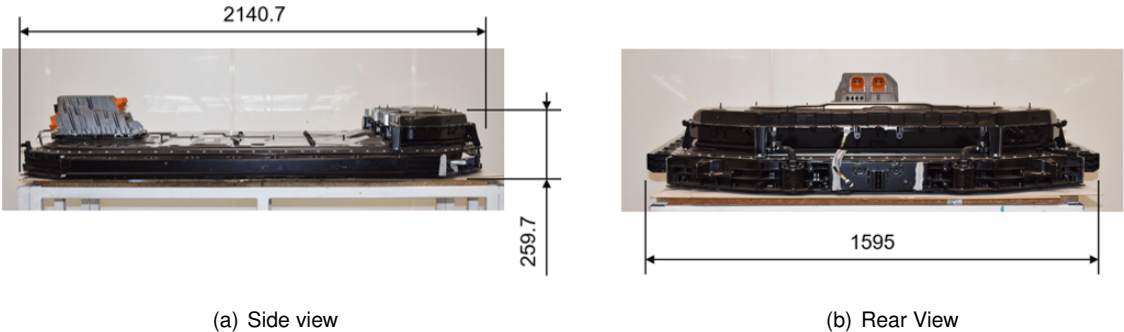
Figure 3.1: Audi E-tron Battery and overall dimensions [38]

</div>
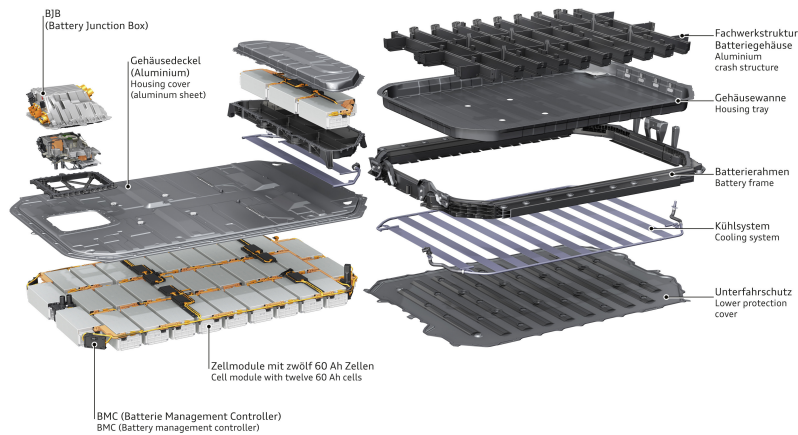
Figure 3.2: Exploded view of the HV-Battery [37] (Courtesy of Audi)

3.2 Battery location

Due to its size, the battery is usually placed in the floor of the car, below the cabin, and spans throughout the entire width of the car. The battery location can be seen in figure 3.3.
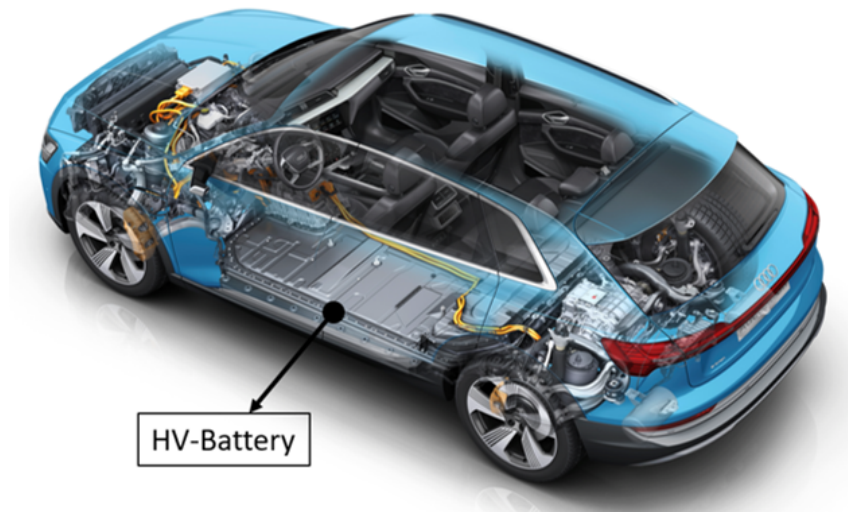
Figure 3.3: Battery location in the Audi E-tron model [37] (Courtesy of Audi)

3.3 Finite element model

The finite element of the battery was developed considering only the most relevant components from the structural point of view. The cooling system, electronic components, junction box (see figure 3.2) and connectors were disregarded. The bolted joints in the model were replaced by rigid elements.

Later on, in section 4.6, the modelling of the connections between the battery and the beams model is addressed. The materials used in this model have customer-specific mechanical properties that will not be approached.

Figure 3.4 shows the entire finite element model of the battery. This assembly contains many sub-assemblies that repeat a large number of times.

The smallest level of this assembly is the cell. Which has a parallelepepidic shape and was modelled with resort to solid elements. It is fixed with rigid elements to the cell module structure in 6 points (see figure 3.5).

Most of the cell module structure is composed by aluminium alloy shell elements. The flanges of the cell module (signaled in figure 3.6 b)) were modelled using solid aluminium alloy elements. Figure 3.6 provides a visual comparison between a render of the actual cell module and the modelled one. Figure 3.7 compares the rendered bolted joint between the cell modules and the battery's floor with the connection used in the finite element model. The latter resorts to a beam element that has a circular cross section with the same diameter as the bolt thread and uses rigid elements to connect the bolt-representative beam element to the flange structure. Figure 3.8 a) shows how a row of 3 cell modules is placed on the floor of the battery. As it is shown in 3.8, there is a glued joint that serves as a continuous connection between the cell module and the module support structure, indirectly connecting the modules to the floor. In the same image, it can also be seen that the cell modules sitting next to the wall of the battery are connected to it via an aluminium alloy bracket, that is signaled in the figure.

Large BEV HV batteries have an energy-absorbing crash structure built into it, which was also included in the model and can be seen in figure 3.9. In this figure, a comparison is done between a render of the actual crash structure and the modelled one. This structure was modelled using aluminum alloy beam elements with a hollow rectangular cross-section.

Figure 3.10 shows the layout of the rear-most cell modules inside the battery's two compartments. Highlighted in this figure, it is possible to see one of the bolt-representative beam elements that connect the roof of the battery (invisible in the figure) to the floor.
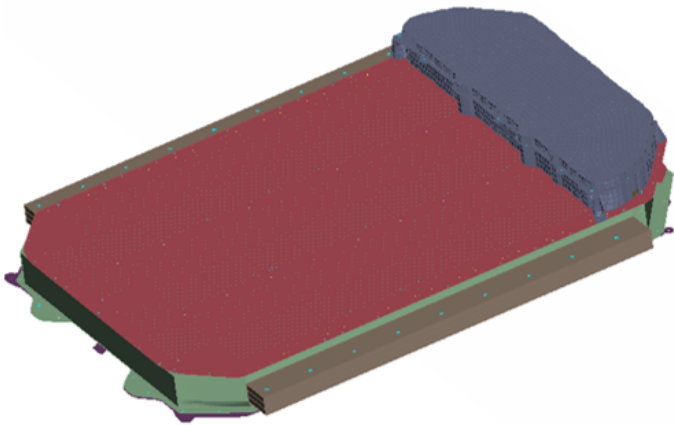
Figure 3.4: Battery finite element model
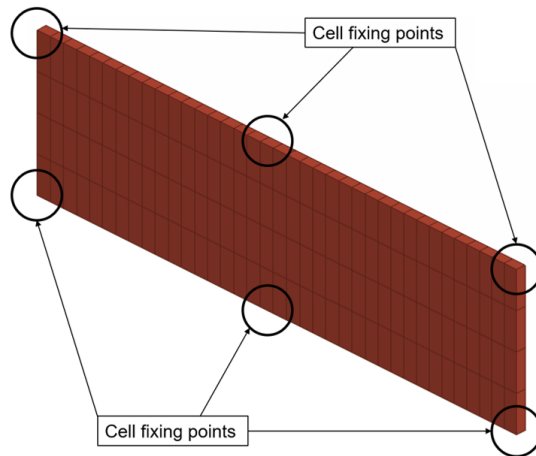
Figure 3.5: Cell module and its fixing points
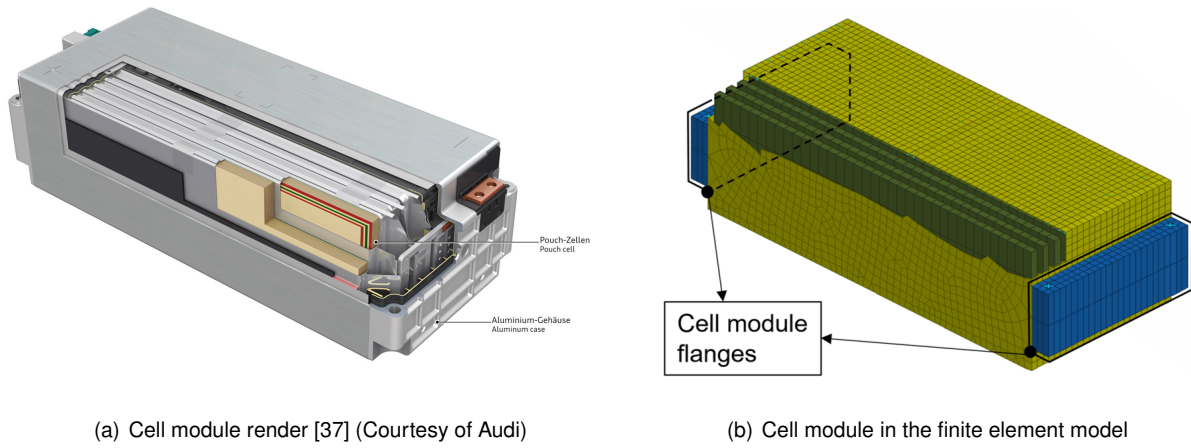
(a) Cell module render [37] (Courtesy of Audi)

(b) Cell module in the finite element model

Figure 3.6: Cell module modelling comparison
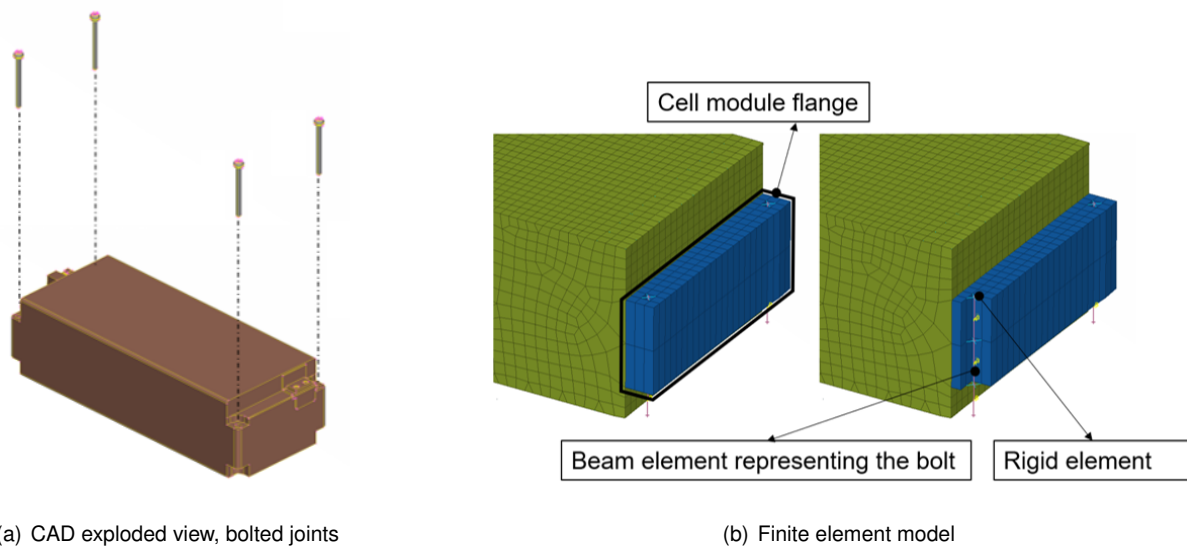
(a) CAD exploded view, bolted joints

(b) Finite element model

Figure 3.7: Cell-module-to-floor bolted joint comparison between the actual rendered connection and the modelled one

(a) Global assembly view

(b) Seam weld detail
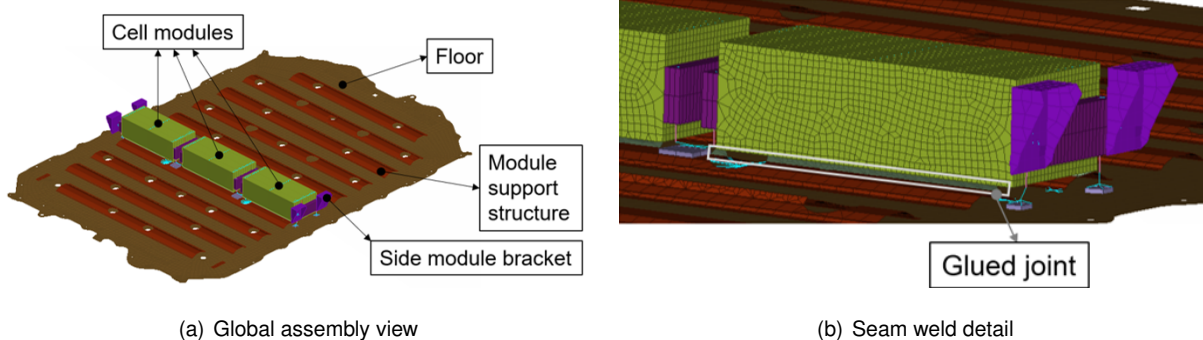
Figure 3.8: 3 of the main compartiment cell modules included in the floor and ribs structure of the battery

(a) Crash structure render [37] (Courtesy of Audi

(b) Crash structure in the finite element model
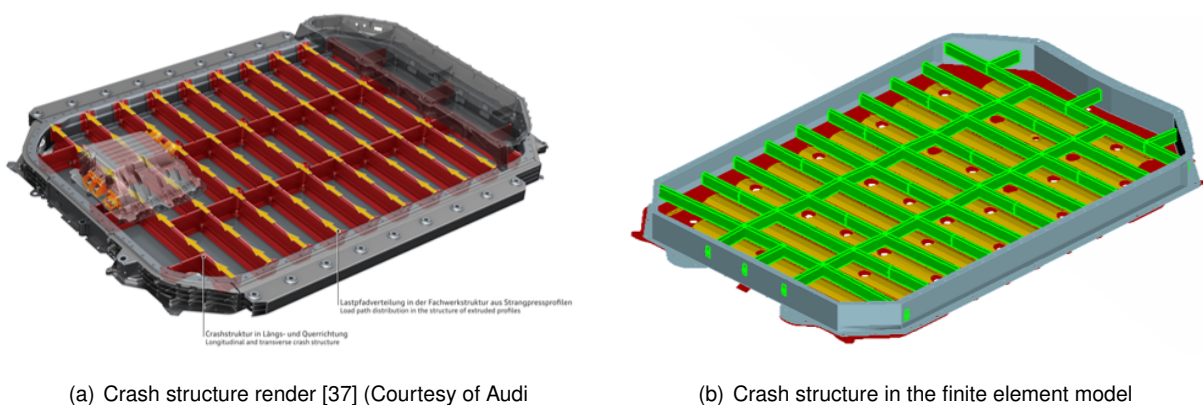
Figure 3.9: Crash structure modelling comparison
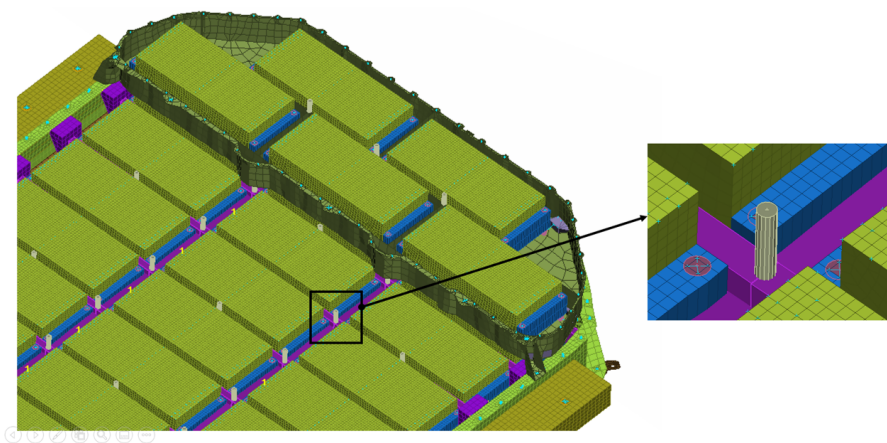
Figure 3.10: Cell module arrangement in the battery compartments and floor-to-roof beam element

3.4   Mass comparison

In this section, a mass comparison between the battery model and the actual HV-battery is done to ensure the similarity of its dynamic behaviour in the multibody simulation. The masses of these components are compared in table 3.1, from which it is possible to see that the mass difference is 1.84 Kg (0.27 %).

Table 3.1: Mass comparison between the actual battery and the finite element model

	HV-Battery	Finite element model
Mass [Kg]	681.26	679.42

3.5 Mode shape comparison

When analysing a component that is subjected to a highly dynamic loading, it becomes relevant to verify its modal properties to ensure that the analysed component behaves similarly to the actual one. In the case of the HV-battery, it is especially important to verify the modal behaviour at lower frequencies, since they are predominant in the multibody dynamic analysis, as it will be concluded in the results presented in chapter 6.

Therefore, a hammer test was performed, from which two mode shapes and the respective frequencies were retrieved. These modes correspond to the first bending and torsion modes of the battery. The hammer test was carried out using rubber mounts under the 4 corners of the battery to better approximate a free-free boundary condition.

Figures 3.11 and 3.12 present the comparison between the two mode shapes. From these figures, it is possible to see that there are local deformations, mainly on the top cover of the battery (flat cover of the main compartment) that are not captured in the hammer test measurements. These local deformations can be observed in the modal analysis results for both the considered modes, but especially in the torsion mode. The main reason for this is believed to be the placement of the sensors. The sensors were placed in a configuration where only global deformations are captured. There is also the possibility that some of the simplifications made when modelling the battery may be originating local deformations. Overall, the main goal of the modal shape comparison is achieved, since the global deformation shape seems to be captured with a high degree of similarity for both modes. Table 3.2 provides a comparison of the natural frequencies for both modes. The maximum relative error is 9.32 %, which is considered acceptable for this purpose, given also the simplifications that were considered in the battery model.

(a) Modal analysis result

(b) Experimental measurement
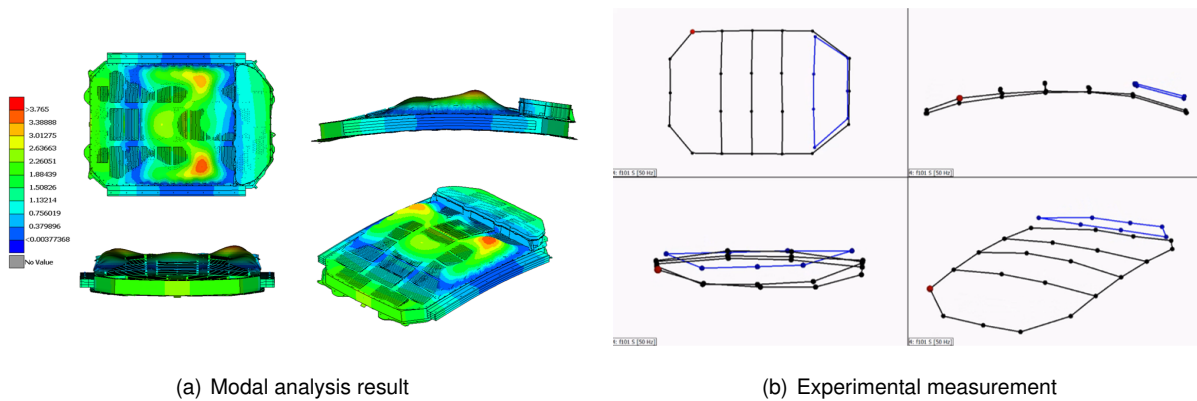
Figure 3.11: 1st bending modal shape comparison

(a) Modal analysis result

(b) Experimental measurement
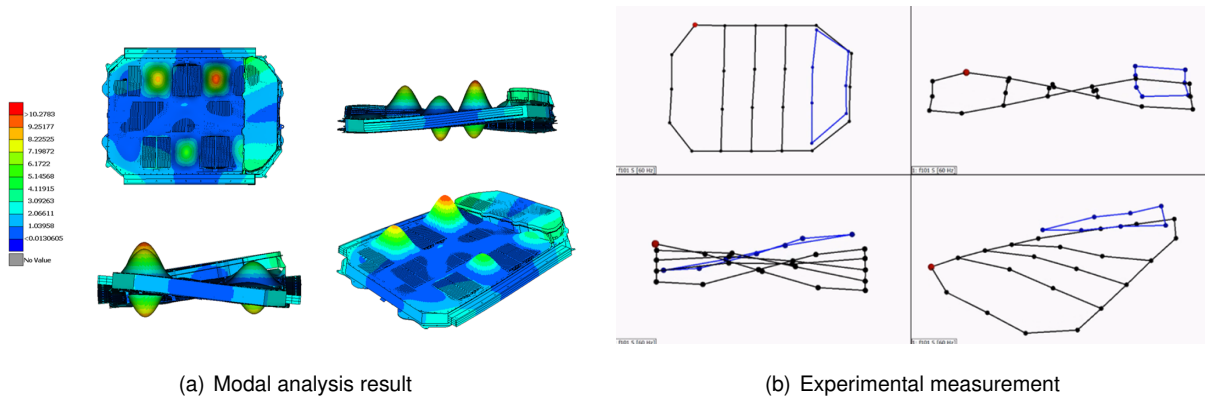
Figure 3.12: 1st torsion modal shape comparison

Table 3.2: Natural frequency comparison for the first bending and torsion mode of the battery

	1st Bending mode	1st Torsion mode
Modal analysis frequency [Hz]	45.34	61.76
Hammer test frequency [Hz]	50	60
Absolute error [Hz]	4.66	1.76
Relative error [%]	9.32	2.93

Chapter 4

Full-vehicle models

The starting point for the full-vehicle model is the suspension model of the Audi E-Tron 55 Quattro Edition One 2019 (see figure 4.1). All the remaining components were imported to this model. The suspension model was used to integrate a flexible model of the chassis structure, in order to create a full vehicle assembly.
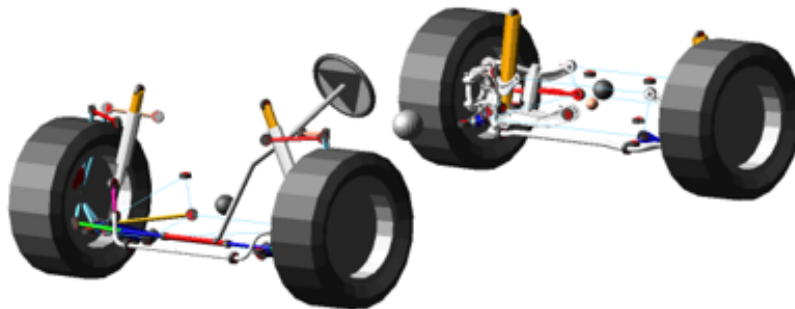
Figure 4.1: Suspension model in Adams Car

For this project, three different types of chassis are addressed:

- **Body in White** : The most complex model of all three, it represents the core structure of the bodywork and disregards moving parts (such as the doors, trunk, bonnet, etc...)

- **Members model** : Includes only the beam features of the BiW model, disregarding the bulky structures of the BiW (such as roof panels, windows, etc...)

- **Beams model**: Consists of a reduction of the members model to an equivalent beams. The 2D and 3D elements existing in each of the load-bearing members of the model are switched to 1D elements with similar cross-sectional properties. This is the only chassis model to take part in the dynamic analyses.

4.1 Body in White

The BiW model is of special relevance to this thesis purpose, since it acts as the interface between the suspension attachments (load source), and the HV battery.

For this dissertation, the Audi Q5 BiW is used. This model has a very good compatibility with the suspension model from Audi E-Tron and only small modifications to the suspension assembly were required to properly fit the BiW model.

(a) Side view

(b) Front view
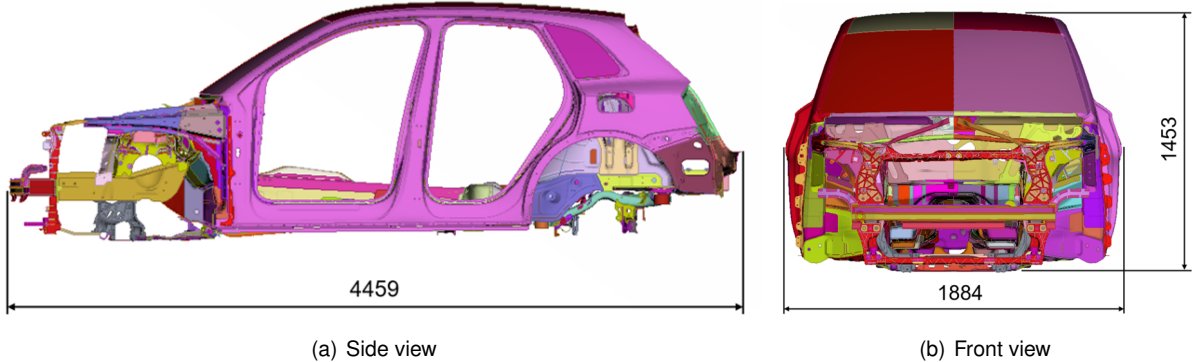
Figure 4.2: BiW model and its maximum dimensions

4.2 Members Model

At very early stages of vehicle development, is is not usual to have detailed information about the chassis of the car. Therefore, using a detailed model of the BiW to analyse components that are attached to it is often not possible.

To tackle this issue, engineers often create simplified models of the BiW with approximated dynamic properties and with just the essential model information to perform a good durability study of these components [39][40]. These simplified models consist of beams models whose beam elements have cross sectional properties that are very similar to the ones of the members they aim to approximate. These beams models are also sometimes combined with a shell structure to account for the panels existing in the structure. Figure 4.3 shows the distinction made between members and panels.
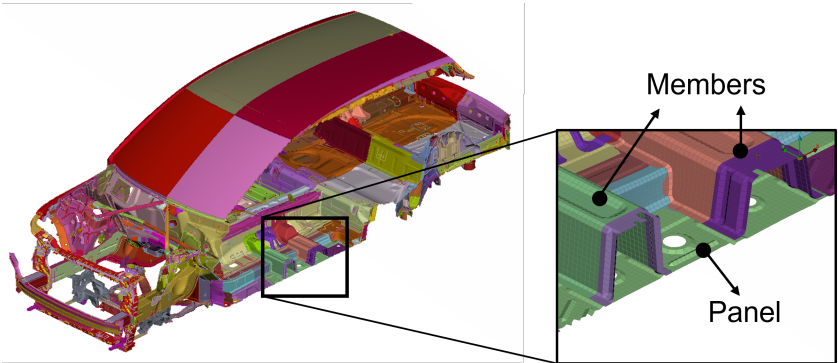
Figure 4.3: Distinction between members and panels in the BiW model

In the case of this dissertation, as a first approach, only the members will be considered and reduced to beam elements to create the beams model. Nevertheless, there is the need to validate the cross sectional properties of the beams. Therefore, an "intermediate" model was created, only considering the members of the BiW model, i.e., the load-bearing structures of the BiW that often have a beam-like shape. This model, hereinafter refered to as "members model" was constructed by removing all the panels from the BiW model, as suggested by figure 4.4
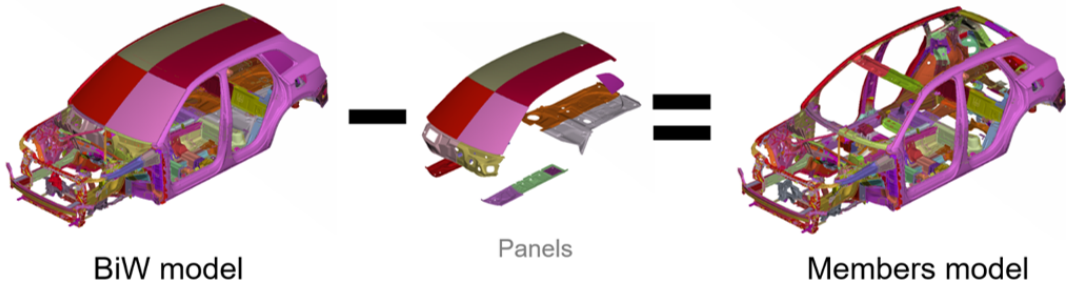
Figure 4.4: Procedure to obtain the members model

4.3   Beams model

Each of the members in the members model now needs to be reduced to an equivalent 1D element. This was done with resort to the *Epilysis* tool available in the ANSA pre-processor [41]. Figure 4.5 provides a schematic description of the members-to-beams conversion, focusing in the specific case of one of the members of the roof frame. For each member in the members model, a *morphbox* was generated. This *morphbox* contains all the elements of the members that should be accounted for in the conversion. Then, a length goal of 150 mm was specified for the beams, and the 1D beam elements were generated. The beams that resulted from the same *morphbox* were automatically connected. The remaining beam nodes were connected manually in all 6 DOF's.
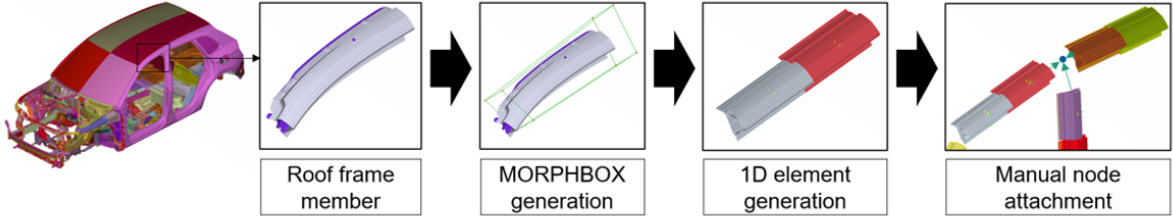
Figure 4.5: Scheme of the members-to-beams conversion

The resulting structure, hereinafter referred to as "beams model" can be seen in the following figure both in simplified view (beam elements only) and detailed view (beam elements with cross section).

(a) Beam representation   (b) Detailed view
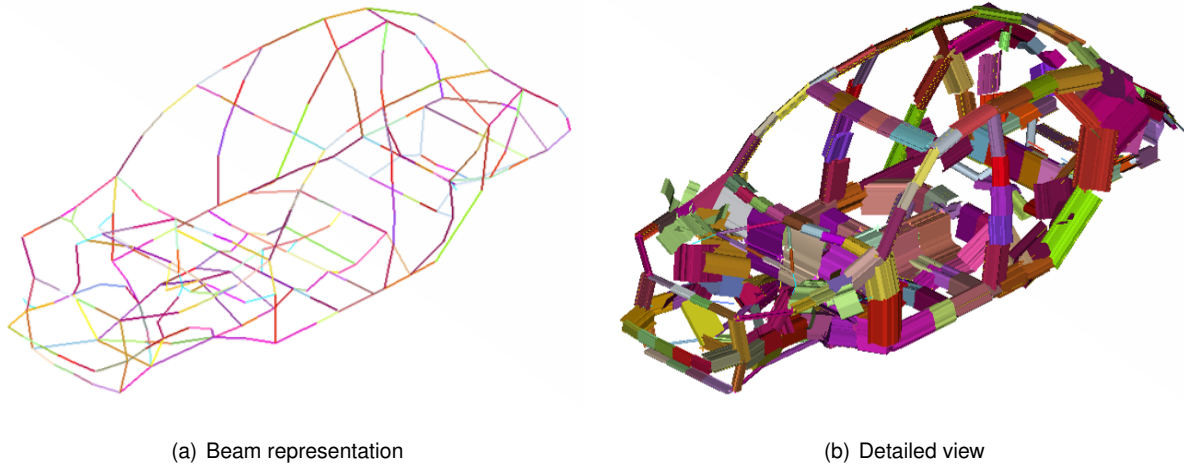
Figure 4.6: Beams model

4.3.1 Cross-section adjustment

The cross sections of the beams model are often composed by multiple metal sheets. The sheets are spot-welded in the flange area creating multiple closed cells within the cross-section. For a better understanding of the structure of the cross-section, figure 4.7 indicates the various regions aforementioned in the specific case of the cross-section of a roof frame beam.

(a) Structure of the cross-section   (b) Metal sheets connected by spot welds [42]
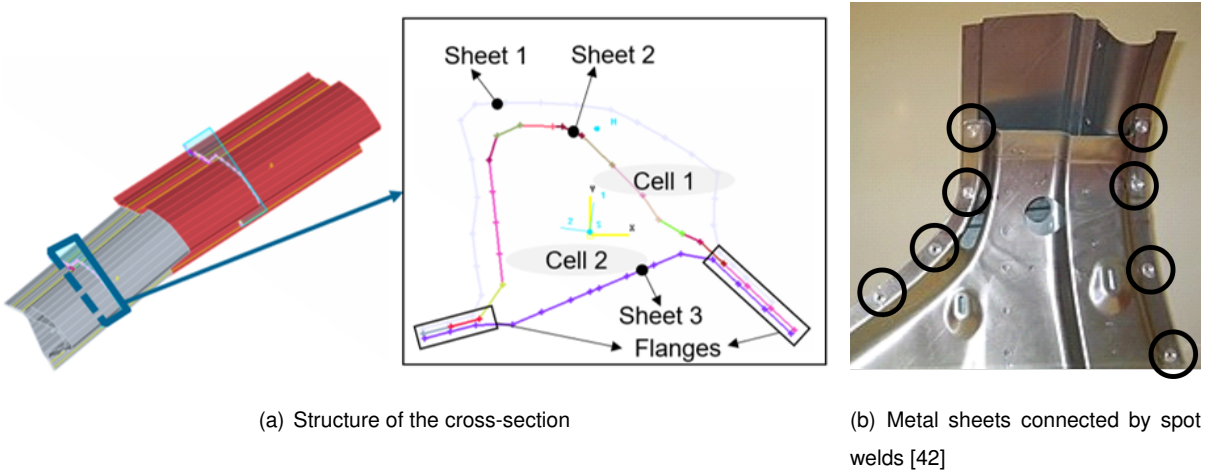
Figure 4.7: beams model

When reviewing the cross-sections of the beams model, it was discovered that some of the flanges weren't actually welded to each other during the 1D element generation process. This aspect would greatly influence the natural frequencies and mode shapes later on in the dissertation. Therefore, the spot welds in the flanges were placed manually. As an effect, the torsion constant increased in more than 200 times, as shown in table 4.1.
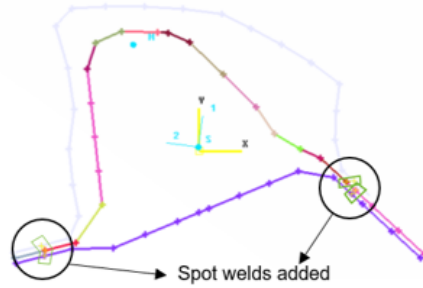
Figure 4.8: Added spot-welds

Table 4.1: Effect of the spot-welds in the torsion constant of the roof frame cross-section

	No spot-welds	Spot-welds added
Torsion constant [mm^4]	537.465	129238

4.4 Comparison between the BiW, Members and beams models

Before moving into more advanced stages of the dissertation, it is important to compare the 3 chassis models mentioned so far, and evaluate the effects of the simplification in terms of number of elements, type of elements and model size. These characteristics are shown in table 4.3 in more detail.

From table 4.3, it is clear that the beams model contains a much lower variety and quantity of elements, therefore affecting the size of the model. The beams model has a size almost 90 000 times smaller than the one of the BiW, meaning that the simulations where the beams model is used will lead to a faster result acquisition, which represents an advantage towards this approach.

Additionally, it is also important to compare the mass of the 3 models, as the mass influences the modal properties of the structures. A mass comparison is made in table 4.2. The reason why the members model has the lowest mass is the fact that the side panels of the car (see figure 4.9) were not included in it, but they were accounted for in the beams model.
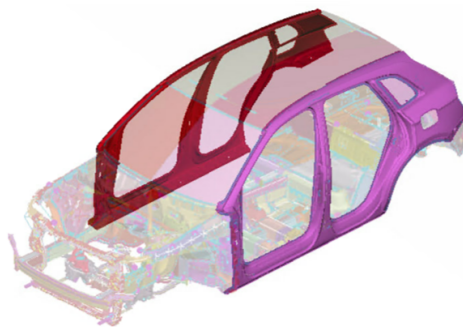
Figure 4.9: Side panels of the BiW

31

Table 4.2: Mass comparison between the BiW, Members and beams model

	BiW	Members Model	Beams Model
Mass [Kg]	526.12	396.93	442.13

Table 4.3: Number and type of elements and size of each of the chassis models.

		BiW	Members	beams
Elements	CBAR	63	59	0
	CBUSH	12	12	0
	CONM2	76	45	0
	RBAR	5	5	0
	RBE2	783	885	46
	RBE3	236 040	165 558	0
	CBEAM	0	8	264
Shells	CQUAD4	705 441	576 083	0
	CTRIA3	44 825	49 961	0
	CTRIA6	136 250	136 250	0
Solids	CHEXA	56 198	47 535	0
	CPENTA	120	16	0
	CTETRA	1 090 203	1 090 203	0
model size [KB]		13 399 376	310 447	152

4.5 MAC Correlation for Beams Model Validation

The beams model will be used as a chassis structure for the multibody dynamic simulation (full-vehicle simulation). For this reason, it is important to ensure that the members model and the beams model have a similar dynamic behaviour, i.e. , similar modal properties (eigenmode shapes and natural frequencies).

The MAC correlation tool available in the META post-processor was used for this purpose. This tool allows the user to import the output files from the modal analysis of the beams and members models to the program so that the comparison is carried. Then, the user must define which nodes from

each structure are considered in the correlation and how they are associated. The nodes used for this correlation can be seen in figure 2.1. The node association is done by importing a .csv file containing the node IDs from the beams and members models as well as the DOFs that take part in the MAC correlation. Only the translational DOFs were considered. For this MAC correlation, the first 6 modes are disregarded, since they correspond to rigid-body modes that do not deform the structures. Starting on mode 7, only the first 6 modes are considered, since the modes with the lowest frequencies are the ones that most participate in the dynamic simulation, as it will be confirmed in chapter 6.

The results of the MAC correlation are output as color-code matrices that associate the modes in the columns (beams model eigenmodes) to the ones in the rows (members model eignemodes). Two matrices are output: one for the MAC correlation, defining mode shape similarity and another one for relative frequency difference. These matrices can be seen in figure 4.10. For the MAC matrix, the closest the cell color is to dark red, the highest the MAC, and the better the mode correlation. For the frequency difference matrix, the closest the cell color is to yellow, the lower the frequency difference, and the better the eigenmodes can be associated.

The goal of the MAC correlation is to check mode shape and natural frequency similarity for modes with the same number. This means that special attention should be given at the results appearing in the secondary diagonal of both matrices of figure 4.10.

(a) MAC matrix   (b) Frequency difference matrix
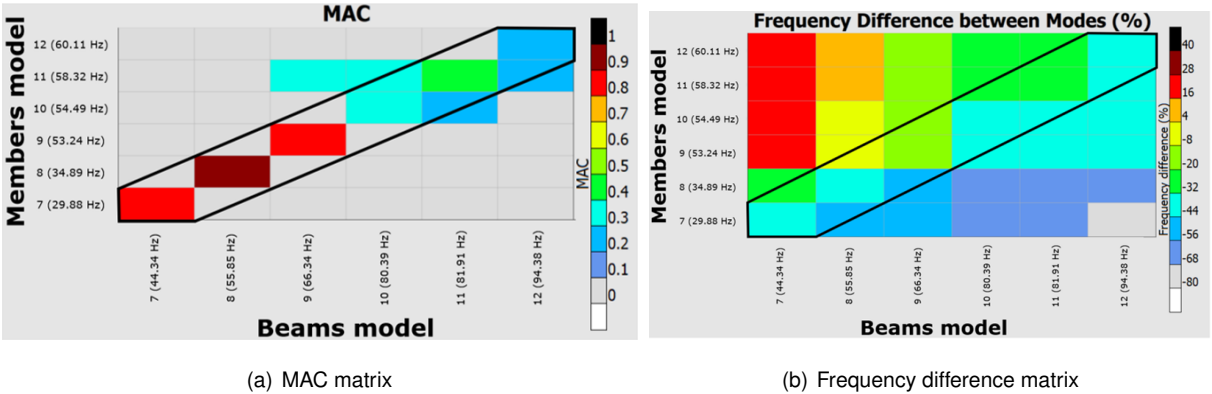
Figure 4.10: Modal Assurance Criterion matrices

From these results, it is concluded that there is a very good correspondence in terms of MAC correlation for modes 7, 8 and 9 (with the MAC value being always greater than 80%). The MAC correlation for modes 10 and 11 is also good, with a MAC value between 30 and 50%. When it comes to mode 12, the structures seem to have a different vibration shape, and therefore, there is not a good MAC correlation is this mode.

From the frequency difference matrix, it can be seen that modes 7, 8, 10 and 12 do not have a similar natural frequency (difference between 32 and 44 %), this difference is due to the fact that the side panels of the BiW, highlighted in figure 4.9 were not included in the members model, but they are considered in the beams model. Because of this, the beams model structure is more stiff, but also heavier, and this affects not only the mode shapes but also the natural frequencies.

4.6 Battery integration in the beams Model

The connections between the battery and the beams model were made via rigid elements. In total, there are 35 connections that, for organization purposes, were divided in 5 different gropus: Front, Top, Side, Top compartiment and Rear connections. The next figures present the location of the different types of battery-to-chassis connections in the actual battery and in the beams model with the battery integrated, hereinafter refered to as beams-battery model.
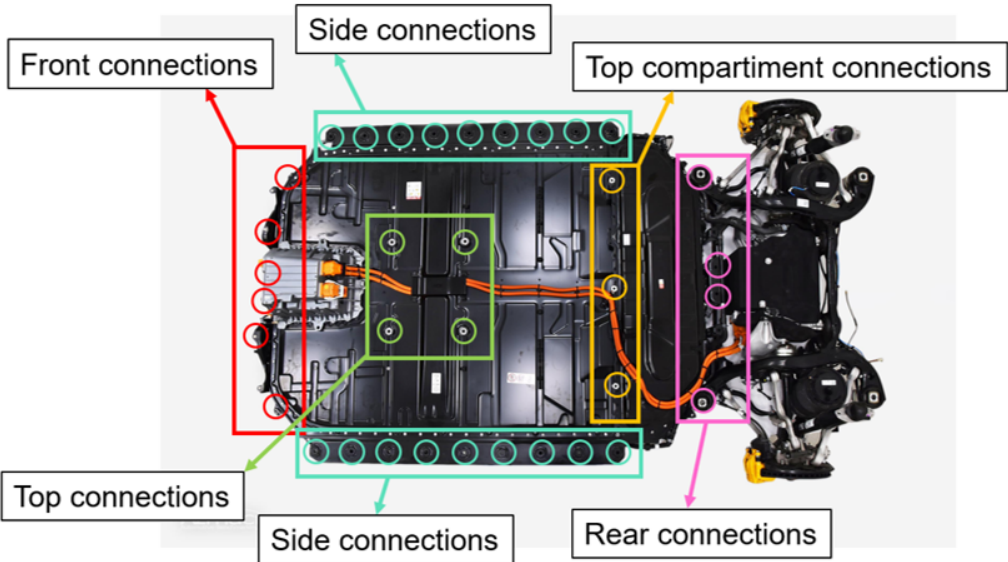
Figure 4.11: Connections signaled in the HV-Battery [38]
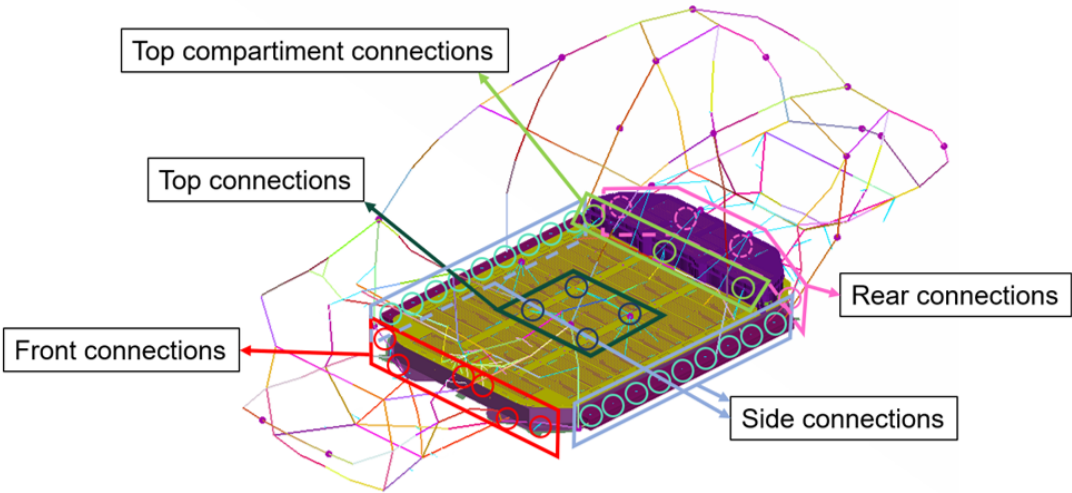
Figure 4.12: Connections signaled in the beams-battery model

4.7 Concentrated masses in the beams model

It is necessary to approximate the mass of the beams model to the mass of the actual loaded vehicle. Therefore, concentrated masses were added to account for the weight that was not previously considered. These masses correspond to components with a low structural role, and therefore, only after the MAC correlation they were integrated in the model. The masses added to the model can be separated in two groups:

- Loaded vehicle concentrated masses: Masses that are part of the car but have a low structural role

- Unloaded vehicle concentrated masses: Passengers and other loads (luggage, etc...)

The mass addition was done by placing CONM2 elements (concentrated mass elements) using the ANSA pre-processor in key-locations demonstrated in figure 4.13. The description and quantity of each type of concentrated mass is also mentioned in the picture. 26 concentrated masses were added, accounting for 11 components.
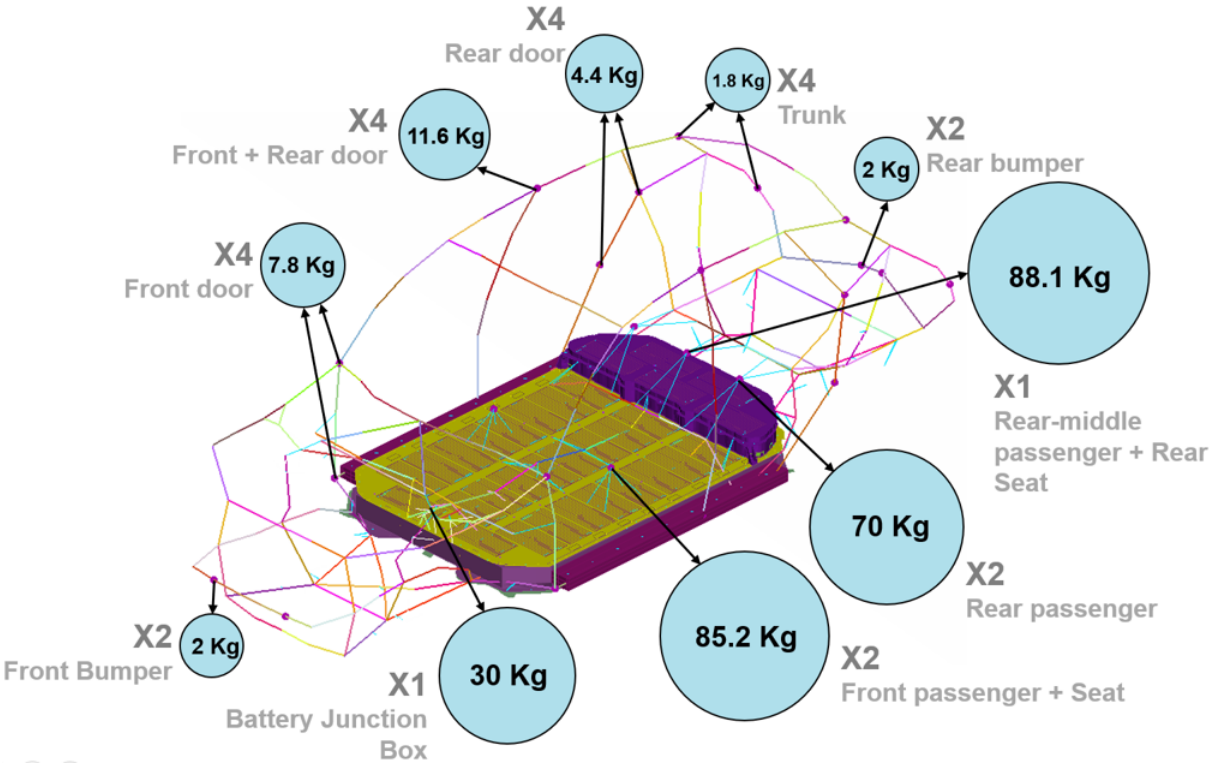
Figure 4.13: Concentrated masses - Locations and mass value

After adding the concentrated masses, the weight of the unloaded beams-battery model and the unloaded BiW-battery model can now be compared, in order to ensure that both structures have a similar mass, therefore improving the coherence of the results. This comparison is made in table 4.4,

from which it is possible to see that the mass difference between both models is 95.29 Kg (7.89%). This is considered to be a small relative difference and, as a result, this value was considered as acceptable.

Table 4.4: Mass comparison between the unloaded beams-battery and BiW-battery models

	Unloaded BiW-battery	Unloaded beams-battery
Mass [Kg]	1208.19	1303.48

4.8   Suspension Model

The suspension model of Audi E-Tron 55 Quattro Edition One 2019 was used as an input for this dissertation. This model was developed in Adams Car 2019.2. Originally, the rear suspension arms and ARB's (anti-roll bars) were defined by flexible bodies, but the rear suspension arms were converted to rigid bodies.

4.8.1   Template-Subsystem-Assembly hierarchy

Full-vehicle assemblies in Adams Car follow a Template-Subsystem-Assembly hierarchy. The template is used to define communicators (i.e. to define connections between the various subsystems) as well as the coordinates of key connection points, known as hardpoints, such as the suspension spring-damper attachments to the chassis. The template also features generic parts that are connected to the hardpoints. Each subsystem references a template file, and inside each subsystem, the generic parts can be replaced by flexible bodies in order to create the actual bodies that take part in the multi-body simulation. The assembly file references all of the subsystems necessary to create the full-vehicle assembly and determines the relative location of each one of them based on the type of template they use. The figure that follows demonstrates a schematic representation of the Template-Subsystem-Assembly hierarchy, focusing on the particular case of the rear suspension sub-assembly.
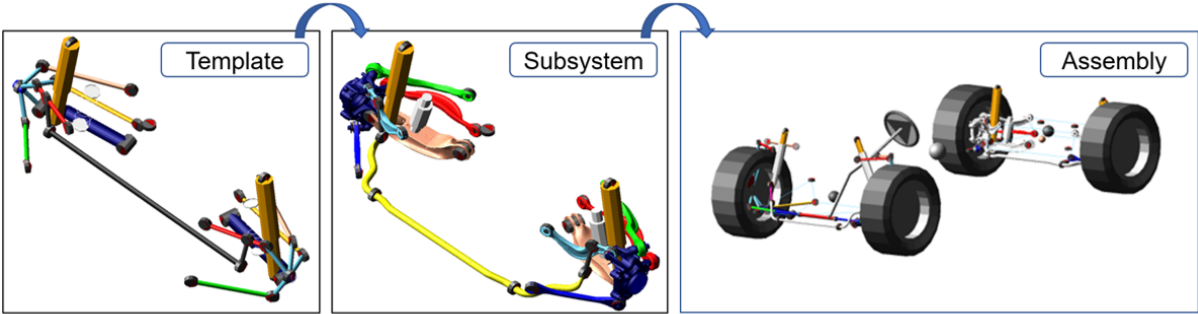
Figure 4.14: Template-Subsystem-Assembly hierarchy for the rear suspension sub-assembly

4.9 Vehicle Model

The following figure presents the vehicle model used in the multibody dynamic simulations. This model results from the assembly of the flexible body of the beams-battery model in the suspension system. The spheres visible in the image correspond to concentrated masses that, similarly to the ones addressed previously, represent mass additions to the unsprung mass of the car, i.e. to the suspension assembly.

(a) Isometric perspective   (b) Side view
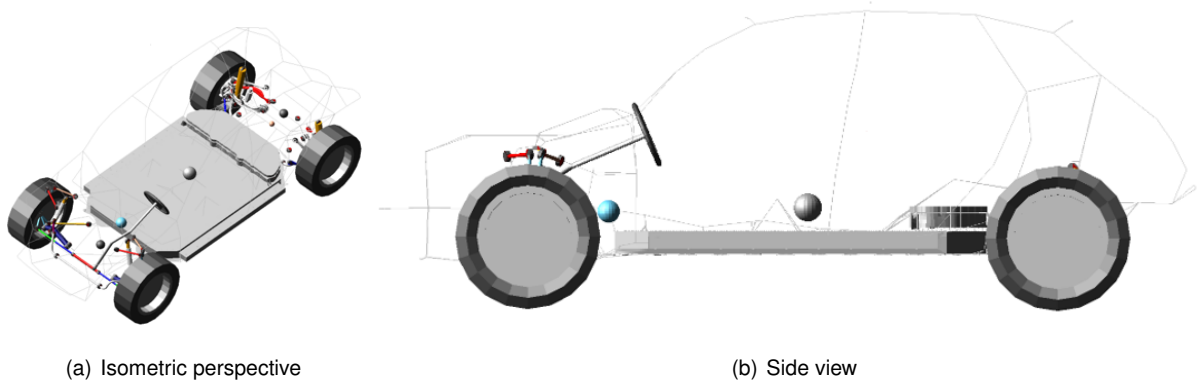
Figure 4.15: Model used in the full-vehicle simulations

Chapter 5

Design of Experiments

This section describes the simulation loop carried throughout the project, the conditions and assumptions used for each of the simulations and which results are intended to be extracted.

5.1   Battery shaker simulation

The battery model generated in ANSA pre-processor was solved using SOL 103 in Nastran (modal analysis request). Together with the modal analysis, the option ADAMSMNF was activated so that a flexible body was exported from the modal analysis in Nastran to the multibody dynamic simulation in Adams View [14]. The modes selected for the modal superposition method were the first 14 modes, i.e., modes 7 to 20, skipping the rigid body modes. A rigid shaker testbed was created and the battery flexible body was attached to it using 26 spherical joints (18 joints in the side, 4 in front, 4 in the rear). The spherical joints were selected instead of the fixed joints due to redundant constraint issues that arose from over-constraining the model. The excitation load was applied to the shaker table via a vertical point motion applied in the center of mass of the shaker table in the positive z direction. The simulation time was set to 10 s, although ISO 12405-1 requires the test to be performed during 21h for one specimen [22]. The reason for this simulation time is the computational effort associated to it. Correctly capturing the vibration of the battery requires a small time step, especially when using an explicit solver like the one in Adams View. The time step chosen for the simulation is 3.125×10^{-4} s, resulting in 32001 steps. Figure 5.1 presents the setup of the battery simulation. In the same figure, it is also possible to see the axis system that was considered.
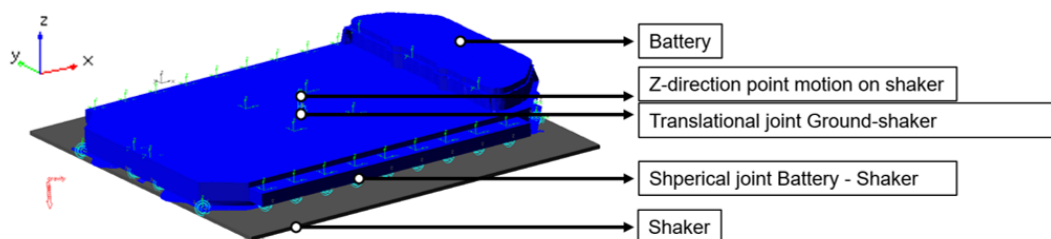
Figure 5.1: Battery shaker simulation setup

5.1.1 Excitation signal derivation

Before applying the dynamic excitation to the shaker table, it is necessary to convert the PSD profile established in ISO 12405-1 to a time signal. For every sampled PSD value, the square root was calculated and a sine-wave signal was generated for each frequency. Each of the sine-waves was set to have a random phase. In the end, all the sine waves were summed and a multiplication factor was applied to correct the units of the signal from g to mm/s^2. The resulting acceleration white noise has a kurtosis coefficient of 1.05, being considered as an approximately gaussian signal as required in standard IEC 60068-2-64:2008 [9]. The crest factor of this signal is 3.49.

If an acceleration time signal was applied to the shaker table in this simulation, there would be no control over the displacement of the table, as there would be no assurance that the second integral (displacement) would have a mean value around 0 mm, which is an important not only as a machinery requirement but also for simulation coherence. Typically, large displacements are caused by low frequency contributions, that, when added to the higher frequency waves, displace the entire signal quite noticeably. Therefore, the displacement time signal was obtained by integrating twice the acceleration signal using the average acceleration method [12] and a bandpass filter was used to eliminate all the frequency contributions below 5 Hz. A flowchart for the acquisition of the imposed displacement time signal can be seen in figure 5.2. The imposed displacement time signal was applied to the shaker table as a spline function of 8001 points interpolated by the Akima method [43].
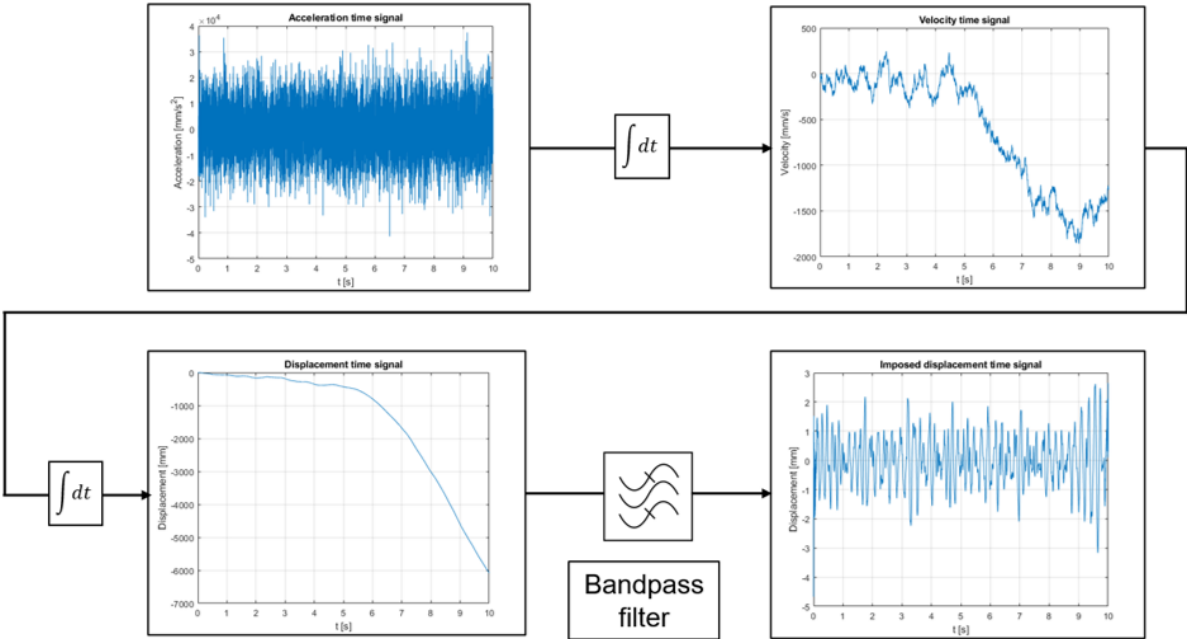
Figure 5.2: Schematic representation of the acceleration-to-time-signal conversion

5.2 Full-vehicle simulations

The full-vehicle simulations consist of a virtual proving ground where the vehicle travels in a controlled straight line across a rough or irregular road. The velocity of the vehicle is maintained constant throughout the simulation. Similarly to the battery case, the flexible body for the beams-battery structure was also exported from Nastran, except that, in this case, the first 27 modes were considered (modes 7 to 34, excluding mode 8). The shape of mode 8 consists of a local deformation on one of the members of the beams-battery model, not deforming the battery. Due to its negligble influence on the battery deformation, this mode was removed from the multibody dynamic analysis. The reason why more modes were selected for the full-vehicle analysis than for the battery shaker test has to do with the frequencies of the modes. In both cases, the maximum mode vibration frequency was set to 200 Hz, as a common practise. Figure 5.3 exemplifies the setup of the vehicle in the simulation. The vehicle is placed in the beginning of a road and moves across it in 10 seconds.
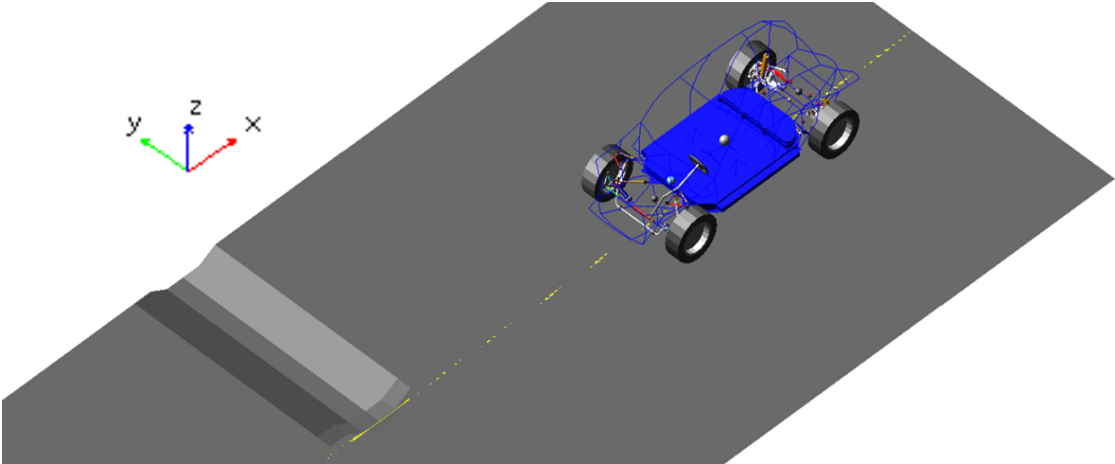
Figure 5.3: Full-vehicle simulation setup
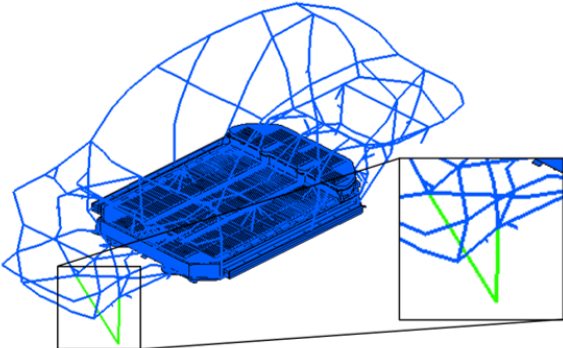
Figure 5.4: Local deformation on mode 8 of the Beams-Battery model

40

5.2.1 Road profiles

The full-vehicle simulations were performed in 5 different virtual proving grounds. The road profiles considered in each of these proving grounds are the following:

- **Pothole road**: consists of a sequence of 5 depressions in the road. The first 2 depressions are located on the right side of the track, the following 2 depressions are on the left-side, and the final one occupies the entire width of the track. Figure 5.6 (a) shows this type of road.

- **D-class road**: This road profile is defined by a gaussian distribution generated from the road's vertical displacement PSD. It belongs to a class of roughness-characterised, non-deterministic roads ranging from class A (smoothest) to class H (roughest). This procedure is established in ISO 8608:2016 [44]. The PSD profile used to define the gaussian distribution is available in figure 5.5. A real-life equivalent of this road can be seen in figure 5.6 b).

- **Washboard In-Phase**: This road profile consists of a sinusoidal signal with an amplitude of 0.025 m (Range of 0.05 m). This signal has a spatial frequency of 1.3 cycles/m [45]. This road is shown in image 5.6 c).

- **Washboard Out-of-Phase**: Similarly to the washboard in-phase, this road profile is also defined by a sinusoidal signal with the same amplitude. In this case, the left and right wheel tracks are placed in opposite phases, so that the peaks of one track coincide with the valleys of the other. This road type is shown in image 5.6 d)

- **Cobblestone road**: Also known as *belgian road*, consists of a division along the x and y axis of a C-class road into blocks with random dimensions. These blocks are spaced from each other, and, due to the non-stationarity of the C-class road profile, spacing the blocks leads to sudden changes in height of the road profile [45]. This road type can be seen in figure 5.6 e)
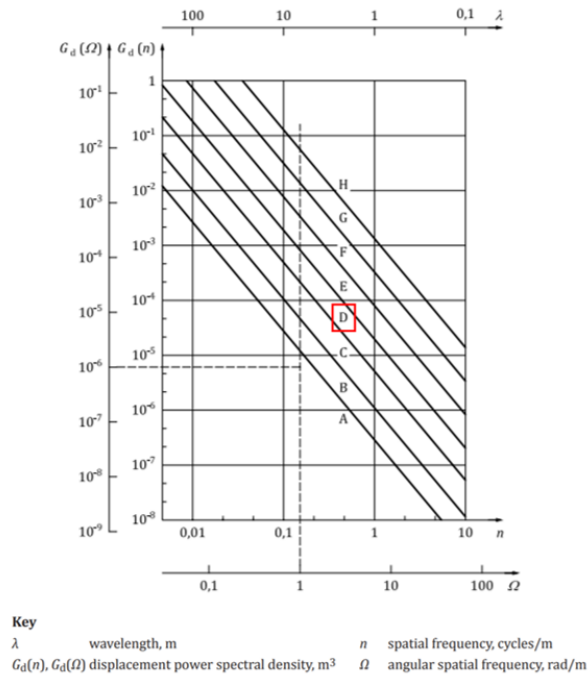
Figure 5.5: Vertical displacement PSD for the various road classes addressed in ISO 8608:2016 [44]

(a) Pothole road

(b) D-class road [46]

(c) Washboard In-Phase [45]

(d) Washboard Out-of-Phase [45]

(e) Cobblestone road [47]
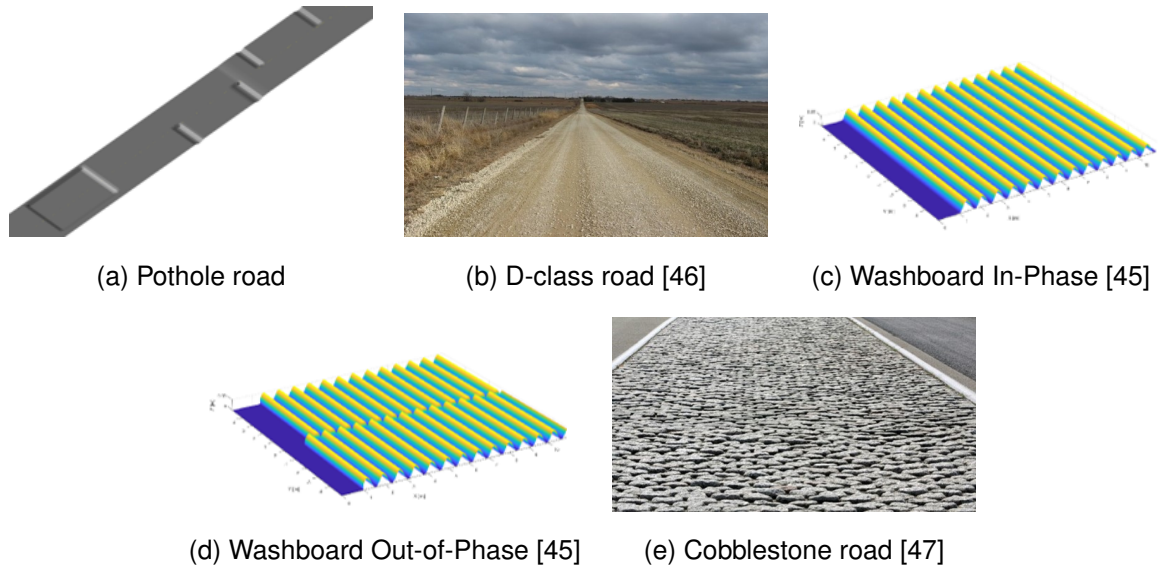
Figure 5.6: Different types of road profiles used

5.2.2 Simulation characteristics

A general parameter for all the full-vehicle simulations (and also for the battery ones) is the simulation time, that was set to 10 s. The full-vehicle simulations were set to have a time step of 0.025 s, resulting in 401 steps.

Due to the different nature of the 5 road profiles considered in this project, the velocities imposed in the vehicle are also different. Table 5.1 summarizes the most relevant characteristics for each of the

full-vehicle simulations.

Table 5.1: Full-vehicle simulation characteristics

Road profile	Vehicle velocity $[Km/h]$	Simulation time $t_{sim}[s]$	Distance covered $d_{sim}[m]$
Pothole	30	10	83.3
D-class road	60	10	166.7
Washboard In-Phase	40	10	111.1
Washboard Out-of-Phase	40	10	111.1
Cobblestone road	40	10	111.1

Chapter 6

Results

This section is dedicated to presenting the final results obtained from the dynamic simulations and experimental measurements. In a first analysis, the modal shapes and MPF's (Modal Participation Factors) will be presented and the first conclusions regarding shapes of deformation will be presented. Then, acceleration measurements obtained from an experimental shaker test on the battery pack will be used for the validation of the acceleration time signals obtained from the shaker simulation. Finally, a pseudo-damage comparison will be carried out, in which the dynamic simulations and the shaker test measurements will be normalized to an equivalent covered distance of 100 000 miles (160.934 Km), so that the damages are compared for an equivalent vehicle usage period. Figure 6.1 provides a visual representation of one of the full-vehicle simulation results. Some of the most critical instants were captured, in which the beams-battery model suffers torsion (frames 81 and 153) and bending (frames 279 and 328). Figure 6.2 presents the deformation of the battery during the shaker simulation.

(a) Frame 81, t = 1.85 s

(b) Frame 153, t = 3.75 s

(c) Frame 279, t = 6.9 s

(d) Frame 328, t = 8.125 s
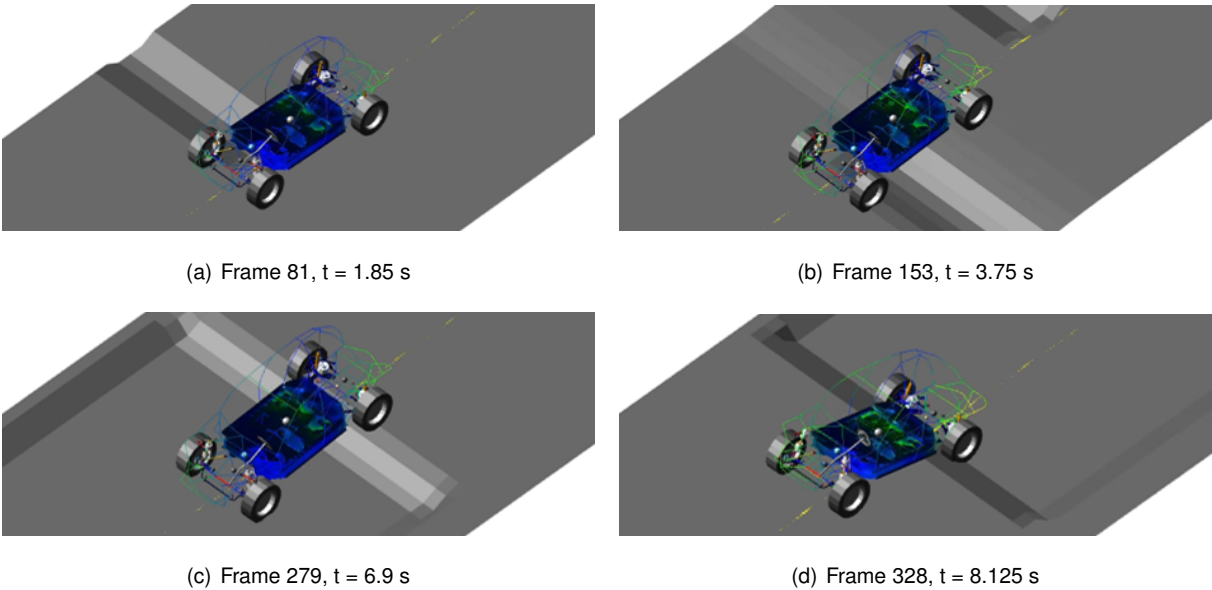
Figure 6.1: Visualization of the beams-battery model deformation during the full-vehicle simulation using the pothole road profile
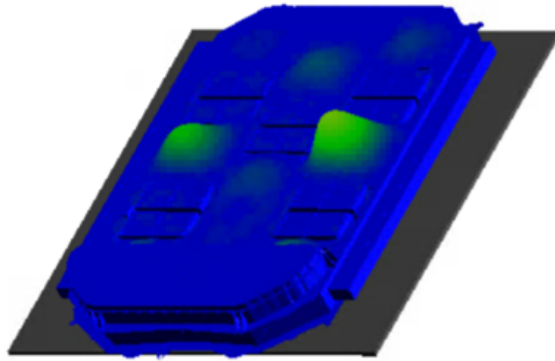
Figure 6.2: Battery deformation during shaker simulation

6.1 Modal Participation Factors

From the multibody dynamic simulations carried out in Adams, the MPF's were obtained as a function of time. Figure 6.3 presents an example of a MPF time signal. The presented MPF corresponds to mode 9 of the beams-battery model.
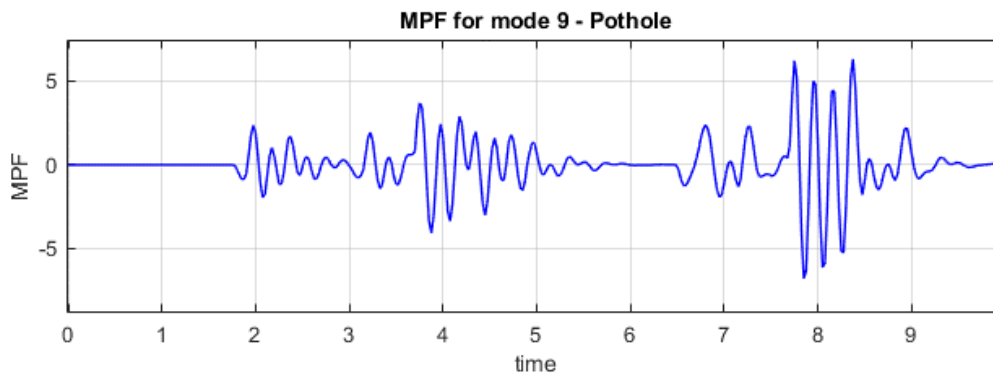
Figure 6.3: MPF time history - Mode 9 of the pothole simulation

It is of particular interest to calculate the RMS (Root Mean Square) value of the MPF's time signal, so that the most participating modes are identified, i.e., the modes with the highest MPF RMS value. Figures 6.4 and 6.5 present the RMS values for the battery and full-vehicle simulations respectively. The 4 most participating modes for the full-vehicle and battery simulation can be found in tables 6.1 and 6.2. Figures 6.6 and 6.7 present the mode shapes of the most dominant modes for the battery model and the beams-battery model respectively.
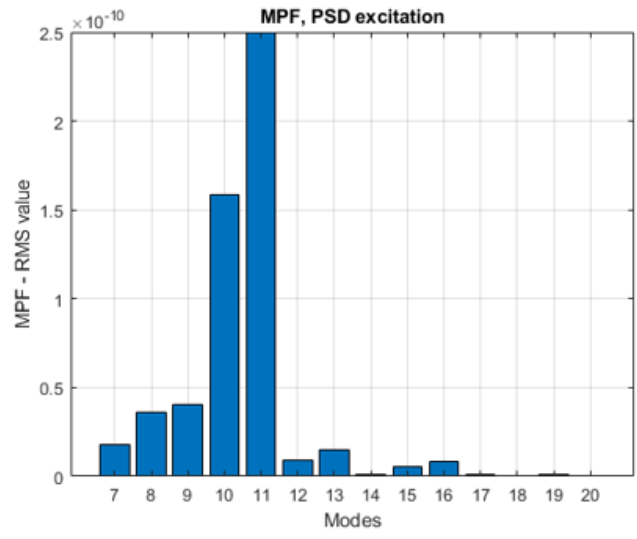
Figure 6.4: RMS MPF values for the Battery shaker simulation
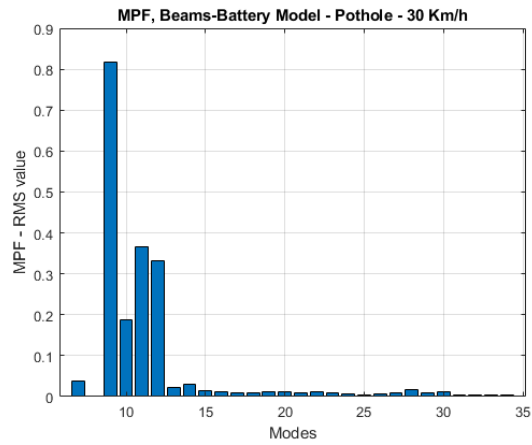
(a) Pothole road
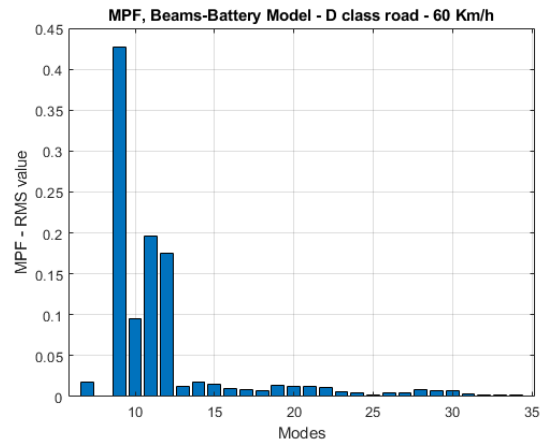
(b) D-class road
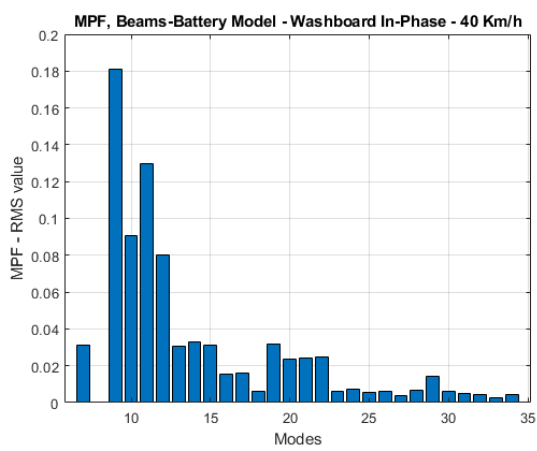
(c) Washboard In-Phase
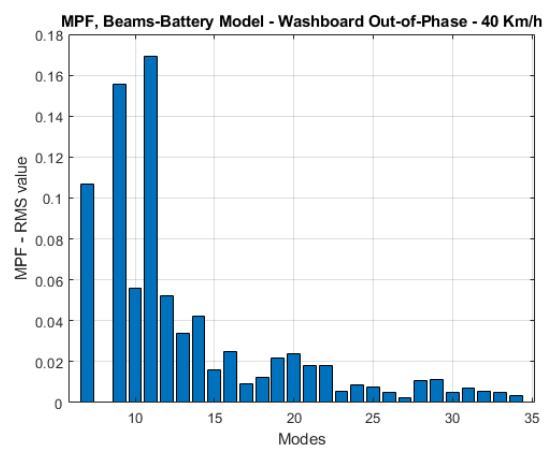
(d) Washboard Out-of-Phase
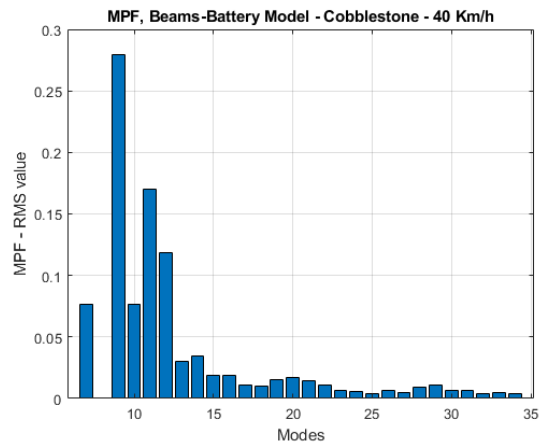
(e) Cobblestone road

Figure 6.5: RMS MPF values of the eigenmodes of the beams-battery model in the full-vehicle simulations

Table 6.1: Full-vehicle simulations: most participating modes for each road type

	Pothole road	D-class road	Washboard In-Phase	Washboard Out-of-Phase	Cobblestone road
1st	9	9	9	11	9
2nd	11	11	11	9	11
3rd	12	12	10	7	12
4th	10	10	12	10	10

Table 6.2: Battery simulation: most participating modes

	Shaker
1st	11
2nd	10
3rd	9
4th	8

6.2 Predominant mode shapes

Figures 6.6 and 6.7 present the mode shapes that dominate the dynamic simulations, based on tables 6.1 and 6.2. Modes 10 and 11 of the battery model contain very high local deformations that were removed from the image so that the global shape of these modes could be shown.

(a) Mode 8

(b) Mode 9

(c) Mode 10

(d) Mode 11
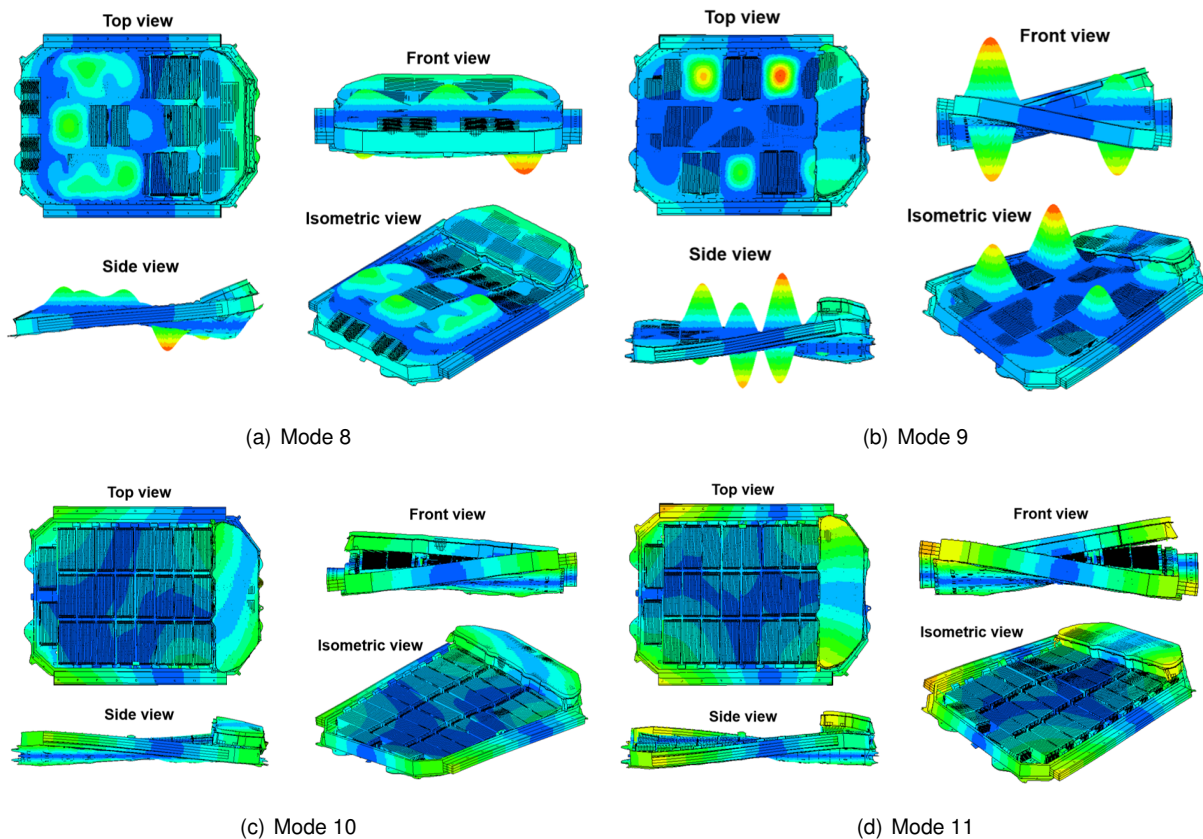
Figure 6.6: Mode shapes of the HV battery model

(a) Mode 7

(b) Mode 9

(c) Mode 10

(d) Mode 11

(e) Mode 12
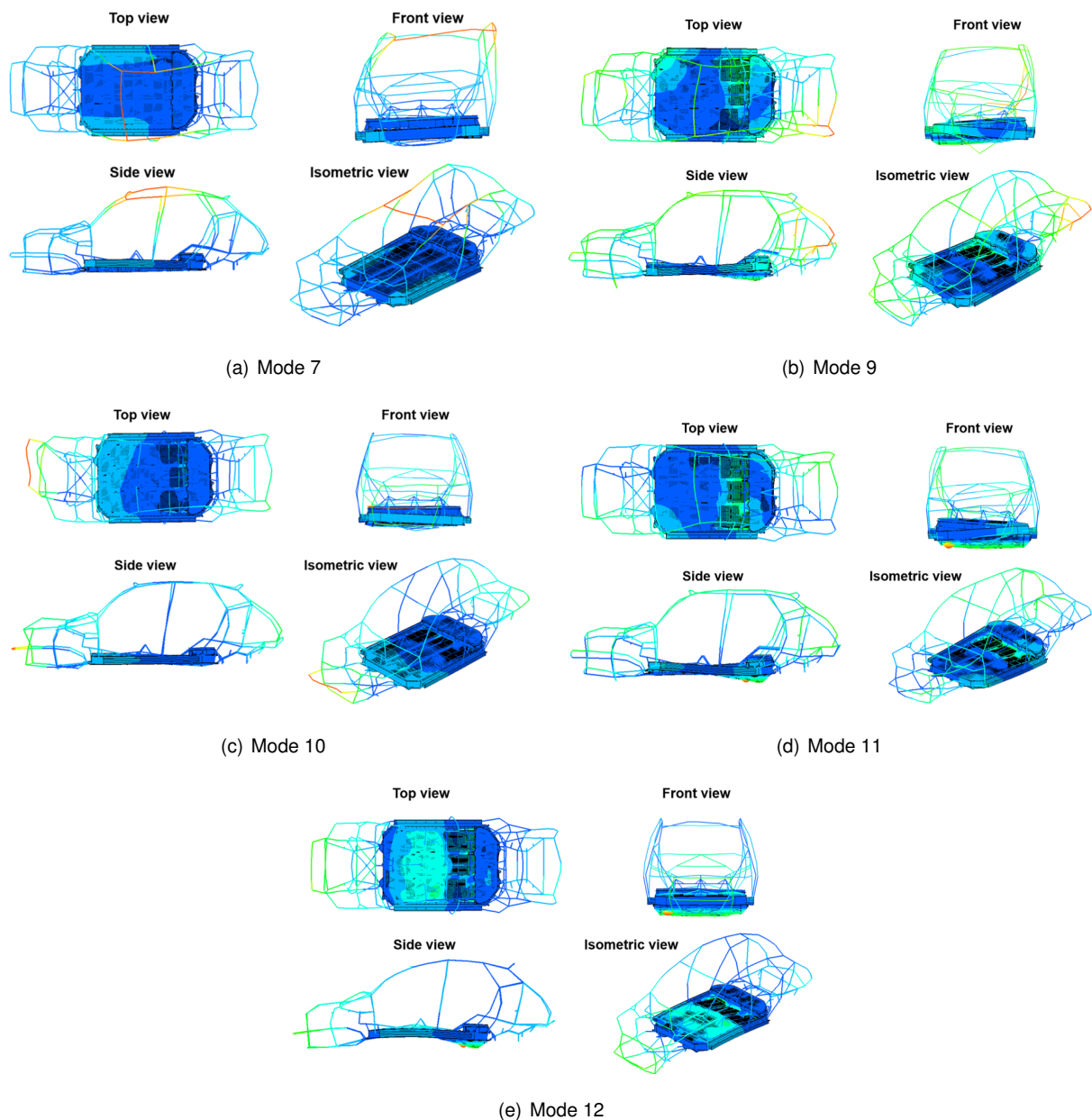
Figure 6.7: Mode shapes of the beams-battery model

6.3 MPF Result Discussion

The battery simulation presents a RMS MPF values in the order of 10^{-10}, indicating that the deformation in the battery pack is extremely low. This can be justified based on the nature of the simulation. The battery is simulated with the same displacement being applied by the shaker testbed in 26 different connections around the battery's perimeter, constraining a large amount of degrees of freedom and preventing large motions. This has an effect in terms of shapes that the battery can acquire. If there is not a mode shape that satisfies a simple constraint condition in the points in which the loadings are being communicated to the battery, it is very difficult to get a meaningful modal participation. This aspect is due to the excess of stiffness characteristic of the shaker test, which is pointed out by Dörnhöfer [6] as the biggest disadvantage of these sorts of tests in BEV HV-batteries, preventing global deformations in

the battery from being captured in the shaker simulation procedure.

The 2 modes that participate the most in the battery shaker simulation are, in fact, torsion modes (modes 10 and 11), actually, mode 11 participates $\approx$ 40% more than mode 10. It should also be noticed that, whether the MPF value of a certain mode acquires a positive or negative value, it is always accounted for in the RMS value as a positive contribution, therefore, some of the mode 11 participation visible in figure 6.4 may actually be due to its symmetric shape. The best way to understand if modes 10 and 11 cancel each other is to look at the MPF's in the time domain and see if the values for modes 10 and 11 are similar at the same instant, which is proved in figure 6.8.
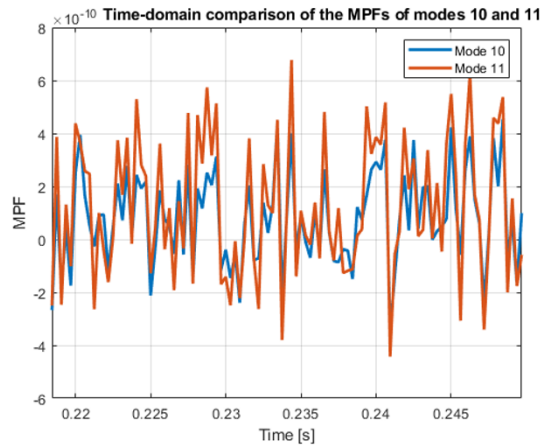
Figure 6.8: Time-domain comparison of the MPF's of the battery eigenmodes 10 and 11

For the full-vehicle simulations, the results here presented show that the highest RMS value of all is verified for mode 9 in the pothole road profile. This is due to the torsion contribution given to the chassis structure when the vehicle passes through the one-sided potholes (see frames 81 and 153 of figure 6.1). In the pothole track, there is also a track-wide pothole that contributes to the bending of the structure. The reason why the torsion contribution appears to be larger than the bending one can be due to the fact that there are 4 one-sided potholes in the track, contributing more significantly to the chassis torsion, and only one track-wide pothole that contributes to the vehicle's bending.

The D-class road also shows a considerable torsion contribution, achieving the 2nd largest overall RMS MPF value with mode 9. From a macroscopic point of view, this is the road profile that presents less irregularities, nevertheless, the roughness of the profile at microscopic level seems to contribute significantly to the deformation of the chassis. Additionally, the velocity at which this simulation is performed is 60 Km/h (twice as much as the one in the Pothole case), which seems to lead to a greater chassis deformation and, therefore, damage. This goes in accordance to the findings in [48], in which the durability function of a BiW presents an exponential decrease with the increase of the travelling velocity.

Between the RMS values of the modes for the washboard profiles, it is possible to see that mode 7 presents a much larger contribution in the out-of-phase than in the in-phase. This is a torsion mode, and is excited when the wheels of the car do not meet the obstacles in similar instants, forcing the car to twist instead. Similarly to mode 7, mode 11 also suffers an increase from the In-Phase to the Out-of-Phase roads, once again contributing to the global torsion of the vehicle.

In the Cobblestone road results, it is possible to see a dominance of torsion modes 9 and 11 over the bending mode 12. This road profile is a "discretization" of a C-class road (rougher than a D-class road), which should increase the mode participation. However, the velocity of the car in the cobblestone simulation is lower than the one in the D-class road, and this appears to have a greater influence on the modal participation results, as the overall RMS MPF values for the cobblestone road are lower than in the D-class road.

In general, by looking at the beams-battery mode shapes in figure 6.7, it is possible to see that the battery pack actually suffers global deformations (torsion and bending), that are not so expressively observed in the shaker simulation due to the high level of constraint of the battery. These global deformations can lead to a shift in the critical area comparing to the one predicted via battery shaker simulation or testing. Additionally, new battery failure modes may arise.

6.4 Acceleration measurements

In engineering applications, whenever possible, simulation results must be compared experimental measurements to strengthen the trustworthiness of the obtained results.

In this dissertation, vertical acceleration measurements from an experimental battery shaker test were obtained. A OEM-specific PSD profile was used for this shaker test that has a strong similarity with the one from the ISO 12405-1 standard. 4 measuring points for this test were selected. They correspond to 4 nodes in the finite element model which have the following ID's: 41000101, 41000148, 41000149 and 41000152. These nodes will hereinafter be referred to by their last 3 digits. Figure 6.9 shows the location of these nodes in the finite element model. The acceleration time signal acquisition process will not be adressed in detail. The most relevant parameters are the duration of the time signal (60 s) and the time-sampling rate (0.00466 s).
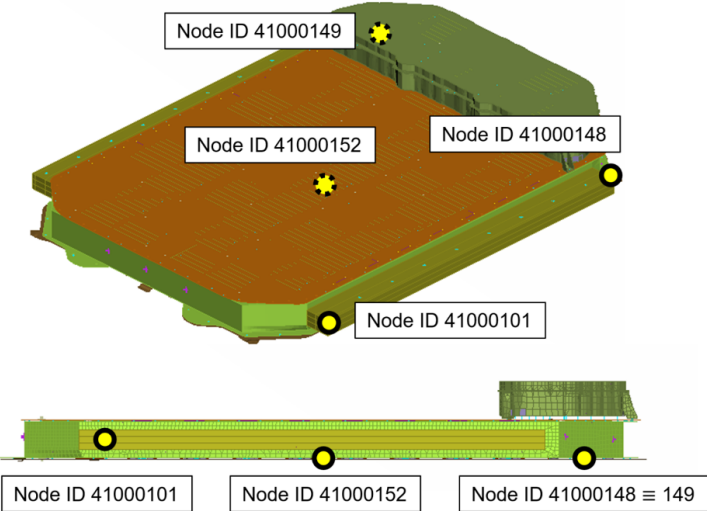
Figure 6.9: Location of the nodes for the acceleration measurement

6.5 Kurtosis coefficient comparison

The following table presents a comparison of the kurstosis coefficient for all the acceleration measurements obtained from the different simulations and also from the shaker test. Since this parameter reveals how different a time signal is from a gaussian one, it becomes important to compare it for the general understanding of the type of loading the battery is subjected to in each of the considered cases. Additionally, and according to the findings in [8], the influence of the crest factor in the pseudo-damage is negligible when compared with the one from the kurtosis coefficient, therefore, only this coefficient is compared.

Table 6.3: Comparison of the kurtosis coefficient (γ_2) for the different vertical acceleration measurements

		Node ID			
		101	**152**	**148**	**149**
Battery shaker simulation		1.05	1.05	1.05	1.05
Battery shaker test		-0.17	-0.12	-0.09	-0.15
Full-vehicle simulations	**Pothole**	12.95	9.04	17.28	17.28
	D-class Road	2.92	0.69	0.83	1.40
	Washboard I.P.	-0.34	0.68	-0.74	-1.14
	Washboard O.P.	31.10	-0.92	-0.61	0.28
	Cobblestone	2.03	1.93	4.65	0.75

From table 6.3, it is possible to see that the kurtosis of the acceleration measurements in the battery shaker test case is almost null, meaning that these acceleration measurements are almost-gaussian time signals, reflecting that the acceleration excitation that is being applied to the shaker during the test is gaussian as well, as requested by standard IEC 60068-2-64:2008 [9]. The battery shaker simulation acceleration time signals show a slightly positive kurtosis, but they are still considered to be almost-gaussian.

From the vehicle simulations, it is possible to see that the majority of the measured signals is leptokurtic ($\gamma_2 > 0$) which goes in accordance to the findings made by Rissoan [8]. The road that appears to be causing the largest kurtosis coefficent values is the pothole, which also generates the largest mode participation. The large kurtosis values for the pothole are due to 2 different reasons: First, there are stages of the simulation in which the vehicle does not drive over an obstacle, instead, it travels in a perfectly flat road between obstacles, which increases the amount of near-zero acceleration measurements at a given simulation time, heavily contributing to zone 2 in figure 2.9. And second, the extreme accelerations measured during the crossing of the obstacles contribute to zones 1 and 3 in figure 2.9. These different situations, when combined together, generate elevated kurtosis coefficients.

Node 152 registers the lowest overall kurtosis coefficients. The reason for this is believed to be the positioning of the node. Unlike the other 3 nodes, node 152 is located in the center of the battery,

therefore, its motion is less affected by the road excitation when compared to other nodes, that are located closer to the suspension attachments.

6.6 PSD comparison

The acceleration measurements and the ones calculated via dynamic analysis will be compared by means of their PSD, since this method allows the frequency content of signals with different durations to be compared, opposite to the fourier transform. The acceleration PSD results will be presented in 4 different figures (one for each node) contained in figure 6.10.

(a) Node 101

(b) Node 152

(c) Node 148

(d) Node 149
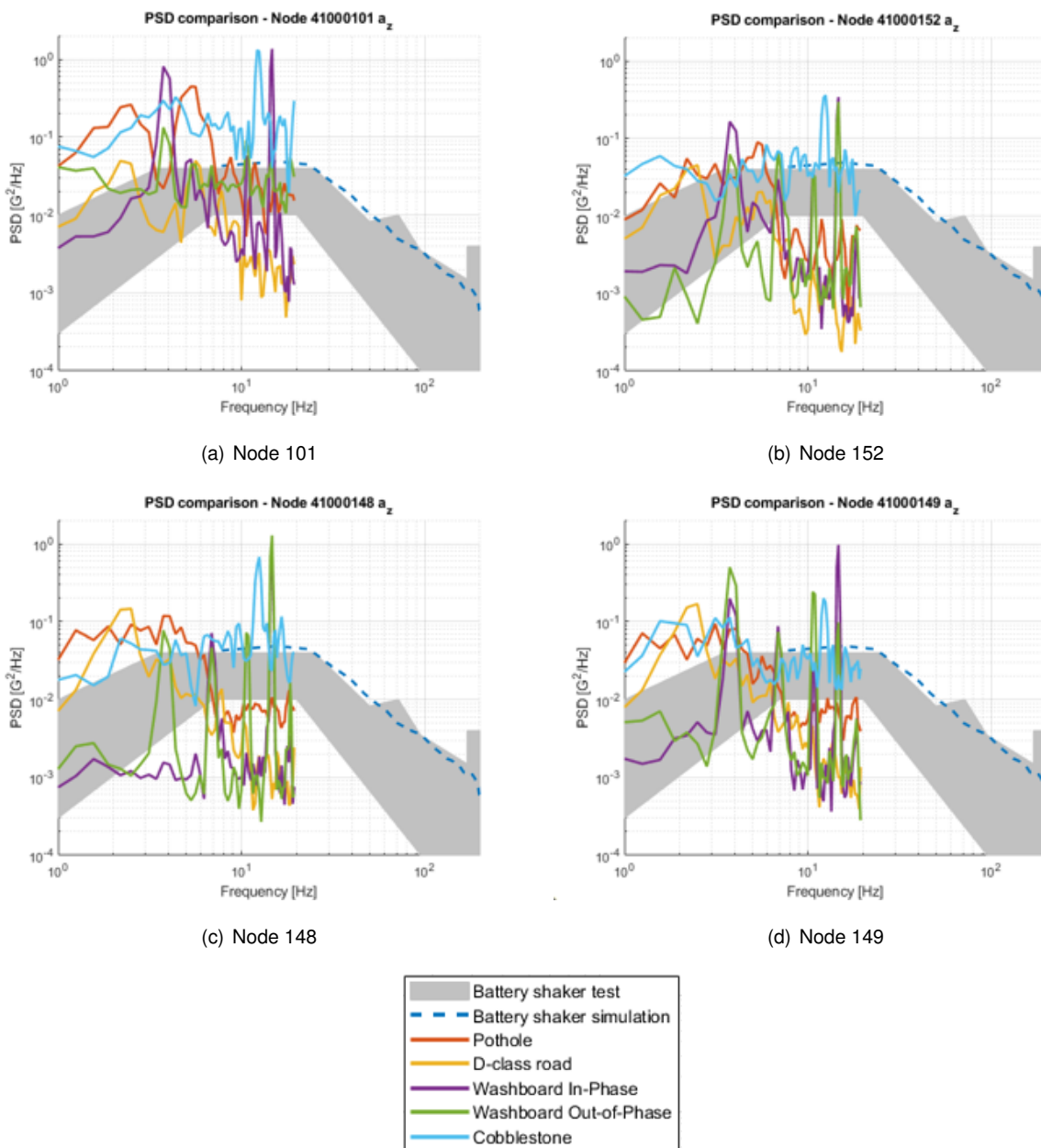
(e) Legend

Figure 6.10: Vertical acceleration PSD comparison

The PSD obtained from the shaker test cannot be explicitly revealed, since it is a customer-specific measurement. However, it is represented in the figure as a grey-colored area that shows only the global shape of the PSD, which is enough to understand that the measured and simulated PSD's are comparable for all 4 nodes.

A characteristic in common to all sub-figures of figure 6.10 is the battery shaker simulation PSD. This profile remains unchanged regardless of the node. This is due to the fact that the battery shaker simulation accelerations are being obtained from nodes that connect to the rigid shaker table where the displacement is being enforced in the battery (nodes 101, 148 and 149). Node 152 is located in the center of the battery, but, due to the low deformations in the component, it ends up having a very similar, almost identical PSD as the remaining nodes. Since these nodes have almost the same displacement over time, the acceleration and the acceleration PSD will also be approximately the same.

By analysing the PSD's acquired from the full-vehicle simulations (solid lines), it is possible to see that there is an overall predominance of the cobblestone road. The pothole accelerations also acquire high values, but mostly at low frequencies (< 8Hz). The washboard in-phase PSD behaves more erratically, assuming noticeable peaks at frequencies above 10 Hz. For nodes 101, 152 and 149, there is cumulative peak at around 4 Hz for both of the washboard roads.

For all the full-vehicle simulation acceleration PSD's, it is relevant to state that the PSD's that show a more erratic behaviour (washboard in-phase, washboard out-of-phase) are also the ones that excite a larger amount of modes at higher frequencies (see figure 6.5) in relative terms. The remaining PSD's show one or two peak values (in the D-class road and pothole cases) followed by a steady decrease; or a constant behaviour with small irregularities (Cobblestone).

All of the full-vehicle acceleration PSD's appear to end at 20 Hz. The justification for this lies in the time step of the dynamic full-vehicle simulations. The time step was set at 0.025 s. On the other side, the eigenmodes of the beams-battery structure that take part in the modal superposition method have a maximum frequency of 200 Hz. By the Nyquist-Shannon Sampling Theorem [49], the lowest frequency sampling rate at which the signal can be sampled is equal to twice the maximum frequency in the signal (≈ 400 Hz). A time step (t_{step}) of 0.025 s leads to a frequency sampling rate of 40 Hz (see equation 6.1). This value not only is lower than the minimum allowed (400 Hz), as it also means that the highest frequency that can be properly represented is 20 Hz (half of the frequency sampling rate), an therefore the limit in the PSD's.

$$\Delta f_{max} = \frac{1}{t_{step}} \tag{6.1}$$

6.7 Acceleration result normalization

In this section, the aforementioned acceleration time signals will be replicated (i.e. sequenced several times) so that all the loadings considered are representative of the same lifetime of the vehicle. The determination of the repetition number is hereby calculated.

In standard SAE J2380 [28], a PSD profile and testing procedure are defined so that the vibration

excitation is tailored to correspond to a loading equivalent of 100 000 miles (160 934 Km) of vehicle usage [50]. However, ISO 12405-1 was not developed to match a specific amount of vehicle usage [29]. Nevertheless, it is a commonly used standard amongst OEM's, and, for that reason, it becomes of special interest to use it in the comparison with the full-vehicle simulations, therefore, the ISO 12405-1 standard will be assumed to be 100000-mile-representative of vehicle usage in this project. This assumption is subjected to a verification of the pseudo-damage generated by both of the aforementioned standards to check whether the damage associated to them is comparable or not. This verification is carried out in section 6.10. It should be noticed that SAE J2380 uses a PSD profile with higher amplitudes ($\approx 0.1 g^2/Hz$ maximum) but a shorter test time (7h57min for the vertical direction), while ISO 12405-1 uses a PSD profile with lower amplitudes ($0.06 g^2/Hz$ maximum) and a larger test time (21h for the vertical direction). This trade-off between PSD amplitude and test duration supports the hypothesis that the damage generated by both standards may be comparable.

The shaker simulation aims at replicating the equivalent of 10 seconds of a random vibration shaker test. Similarly, the vertical accelerations in the shaker test were measured for 60 s.

On the other hand, for the full-vehicle case, each of the performed simulations covers a distance of 83.3, 111.1 or 166.7 m, depending on the road profile (see table 5.1).

For both cases, there is a necessity of extrapolating the results to comparable distances. This is achieved by replicating the acceleration time signals from all dynamic simulations and measurements a certain number of times until they match in terms of covered distance. The goal distance was set to 100 000 miles, which is a value used for similar purposes in other studies [29][50]. The battery simulation accelerations are left out of this comparison, since the simulated PSDs present much lower values than the measured ones, suggesting that the pseudo-damage generated by the simulated PSD is lower and upper-bounded by the one from the shaker test. For this reason, the measurements from the shaker test will be used instead.

For the battery shaker test measurements, the 60 second vertical acceleration time signals will be replicated 1260 times to make up 21h of uni-direccional random vibration testing.

For the full-vehicle simulations, the situation is more complex. Each of the road profiles needs to be averaged according to regular procedures used by vehicle constructors. When it comes to experimental vehicle durability testing, OEM's resort to proving grounds that have several diferent types of roads available (see figure 6.11).

Figure 6.11: Bad Road area at Zalazone Proving Ground, Zalaegerszeg, Hungary [51]

OEM's specify which road profiles the vehicle should be tested on and the participation percentage of each road profile in the overall vehicle testing circuit length. An example of these participation percentages can be found in [29]. In this study, the 5 road profiles considered in this thesis take part in the vehicle testing circuit and their participation is summarized in table 6.4. The final participation to make up the 160 934 Km (100 000 miles) target is also calculated and presented in the table. The number of times each of the full-vehicle simulations needs to be replicated is presented in table 6.5.

Table 6.4: Distance covered in every road for the 100 000 mile goal

Road profile	Testing distance [Km]	Percentage participation [%]	Final participation [Km]
Pothole	0.16	4.32	6958.8
D-class road	0.16	4.32	6958.8
Washboard In-Phase	0.64	17.30	27836.8
Washboard Out-of-Phase	1.29	34.87	56109.6
Cobblestone road	1.45	39.19	63068.4
Total	3.7	99.99	161032.4

Table 6.5: Calculation of the number of repetitions for each of the vehicle simulations

Road profile	Track length [m]	Final participation [Km]	Number of repetitions
Pothole	83.3	6958.8	83539
D-class road	166.7	6958.8	41744
Washboard In-Phase	111.1	27836.8	250556
Washboard Out-of-Phase	111.1	56109.6	505037
Cobblestone road	111.1	63068.4	567672
Total	583.3	161032.4	1448548

6.8 Pseudo-Damage calculations

The pseudo-damage concept is applied to the time history of the vertical acceleration time-signals of 4 nodes of the HV-Battery, the node ID's range from 41000101 to 41000152. The nodes locations can be seen in figure 6.9

The load cycles within each acceleration time-history are counted with resort to the rainflow counting method [31]. The result of the load cycle count in each acceleration time signal is a rainflow matrix, that presents a division of the cycle count in terms of their mean value and range. An example of a rainflow matrix is presented in figure 6.12. The β exponent in expression 2.14 is considered to be 5 as a thumb rule defined in [31] for chassis mounted components. For purposes of rainflow count and damage calculation, the WAFO MatLab toolbox was used [52].

Figure 6.13 presents the pseudo-damage results for the equivalent of a 100 000 mile covered distance. The results are presented in a logarithmic scale for better comparison between the full-vehicle and battery shaker pseudo-damage. The pseudo-damage from the different roads in the vehicle simulations was accumulated for each node and compared to the one from the shaker test. The simulated acceleration time signals do not take part in the pseudo-damage calculations, as the PSD predicts that the damage from these signals should be negligible when compared to the measured accelerations pseudo-damage.
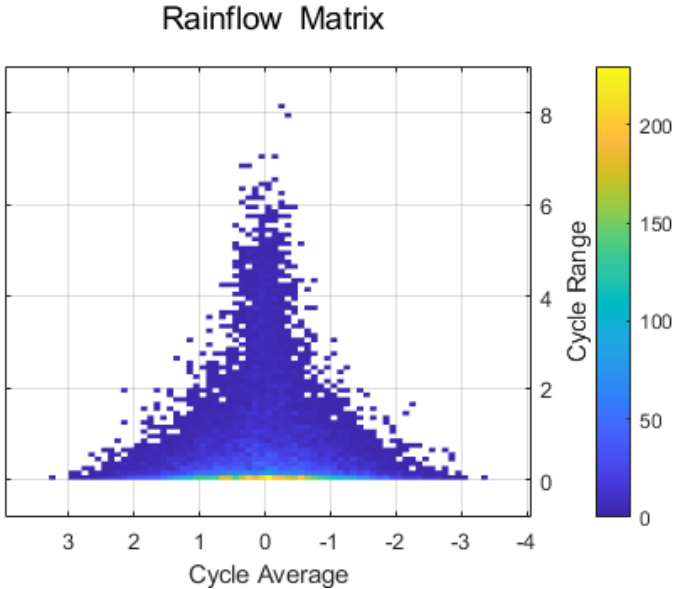
Figure 6.12: Rainflow matrix for the acceleration time signal acquired from the shaker test for node 101
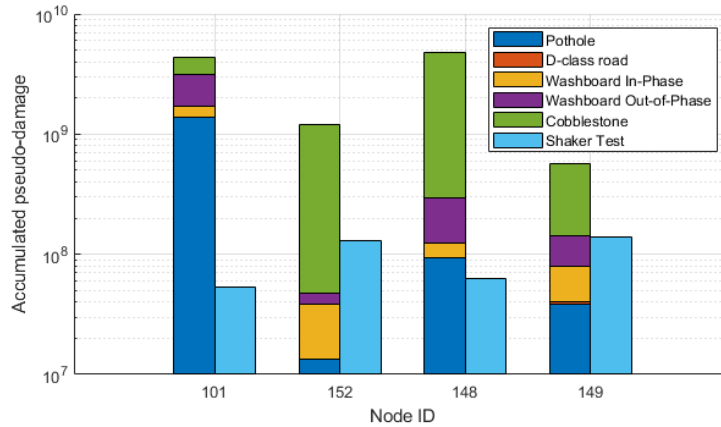
Figure 6.13: Accumulated pseudo-damage comparison betweeen the full-vehicle simulations (left stack) and the battery shaker test (right stack)

From the graph of figure 6.13, it is possible to see that, for all nodes, the pseudo-damage generated from the full-vehicle simulations is greater than the one from the shaker. Nevertheless, the following tables present the pseudo-damage contribution from each road type for each node in absolute terms (table 6.6) and relative terms (6.7). In table 6.7, the results presented are the pseudo damage from each road type divided by the battery shaker test pseudo-damage. The last row of the table presents a scaling factor for the vehicle simulation pseudo-damage with respect to the one from the shaker test. In both tables, the highest and lowest results for each node are highlighted in red and green respectively.

Node ID		41000101	41000152	41000148	41000149
Battery shaker test measurements Pseudo-damage		5.39E+07	1.28E+08	6.35E+07	1.38E+08
Vehicle simulations Pseudo-damage	Pothole	1.37E+09	1.33E+07	9.32E+07	3.88E+07
	D-class road	2.70E+06	2.09E+05	1.27E+06	1.57E+06
	Washboard I.P.	3.46E+08	2.47E+07	3.03E+07	3.92E+07
	Washboard O.P.	1.44E+09	9.02E+06	1.72E+08	6.34E+07
	Cobblestone	1.16E+09	1.16E+09	4.45E+09	4.31E+08
	TOTAL (Vehicle simulations)	4.32E+09	1.21E+09	4.75E+09	5.74E+08

Table 6.6: Absolute Pseudo-damage contribution from each type of road $[g^5]$

Node ID		41000101	41000152	41000148	41000149
Vehicle simulations Pseudo-damage	Pothole	25.42	0.10	1.47	0.28
	D-class road	0.05	1.63E-03	0.02	0.01
	Washboard I.P.	6.41	0.19	0.48	0.28
	Washboard O.P.	26.73	0.07	2.70	0.46
	Cobblestone	21.51	9.04	70.13	3.12
	TOTAL	80.12	9.40	74.80	4.16

Table 6.7: Relative Pseudo-damage contribution form each type of road

6.9   Pseudo-Damage result discussion

From the results presented in the previous section, it is possible to conclude that there is a clear difference between the pseudo-damage in both situations. In the vehicle simulations, the pseudo-damage generated is 4.16 to 80.12 times larger than the one from the shaker test.

The road type that mostly contributes towards the vehicle simulations pseudo-damage is, generally, the cobblestone road. This road type does not generate the highest mode participation (see figure 6.5), but it has the largest amount of repetitions in the 100 000 mile test track (see figure 6.5) and generates some of the largest PSD values (see figure 6.10), therefore justifying why this road type ended up as being the most damaging one. By looking at the PSD's from figure 6.10, it is possible to see that all road types present, in general, a descent when approaching the 20 Hz frequency. The only PSD profile that does not follow this trend is the cobblestone one. This means that, if larger frequencies were able to be captured, the PSD profile for the cobblestone road would still show considerable high values, therefore bringing a considerable additional damage contribution. In practice, this means that, despite the fact that the pseudo-damage in the vehicle simulation is larger than in the battery shaker test, it appears to be underestimated.

6.10   Pseudo-damage comparison : ISO 12405-1 vs. SAE J2380

Earlier in this dissertation, in section 6.7, the assumption that the pseudo-damage from standards ISO 12405-1 and SAE J2380 is the same was made.

In this section, it is intended to verify if the pseudo-damage generated by both of this standards can actually be compared.

This is done by importing each of the standardized PSD profiles to the Vibration data toolbox [53] from which a stationary white noise acceleration time signal is obtained. Once again, only the vertical direction of each PSD profile is considered. Each of the retrieved time signals has a duration of 10 s, and they had to be sequenced to make up for 21h of vibration testing in the ISO 12405-1 case and 7h57 min in SAE J2380, similarly to what was done in section 6.7. The number of repetitions for each time signal is shown in table 6.8. From these replicated time signals, the pseudo-damage was calculated with resort to the WAFO MatLab toolbox [52]. The cumulative pseudo-damages generated by the vertical excitation accelerations in both of the standards is highlighted in table 6.10. In the SAE J2380 standard, 3 different vertical vibration PSD profiles are applied in sequence to the battery. Therefore, the pseudo-damage generated by the three of them is summed and taken as the total pseudo-damage generated from the SAE J2380 shaker test.

Table 6.8: Pseudo-damage comparison: ISO 12405-1 vs. SAE J2380 standardized acceleration excitation load.

		time signal duration [s]	test duration [h]	No. of repetitions	Pseudo-damage $[g^5]$
ISO 12405-1	z-direction	10	21	7560	2.94×10^8
SAE J2380	vertical 1	10	2.65	954	2.27×10^8
	vertical 2	10	2.65	954	2.49×10^8
	vertical 3	10	2.65	954	2.01×10^8
TOTAL (SAE J2380)		-	7.95	2862	6.77×10^8

From the table above, it is possible to conclude that the pseudo-damage generated from the PSD-derived acceleration time signal established in standard SAE J2380 is 2.3 times larger than the one of the ISO 12405-1 standard. This suggests that, even if the SAE J2380 standard was used in the HV battery shaker simulation, it would still not generate as much damage as the vehicle-level simulations (since the full-vehicle simulations are, at least, 4 times more damaging than the battery shaker test that was performed in accordance to ISO 12405-1). However, it should be noted that this section provides a very rough comparison between the HV battery testing standards, since the accelerations under comparison here are the actual standardized acceleration excitations and not acceleration measurements retrieved from certain locations in the battery.

Chapter 7

Conclusions

A brief summary of the objectives established in chapter 1 is here done:

- To develop a simplified truss model with similar modal properties as the detailed BiW model.

- To determine and compare the mode shapes that dominate the dynamic analyses and modal participation in them.

- To measure and compare the accelerations obtained from the dynamic simulations and shaker test.

- To calculate and compare the acceleration-based pseudo-damage generated from the full-vehicle simulations with the one from the battery shaker test.

7.1 Achievements

A truss model was developed to replace the BiW model in the vehicle simulations. This model leads to a much smaller computational effort whist having a similar dynamic behaviour as the BiW model, especially for lower frequencies.

An acceleration time signal was generated from the PSD profile defined in ISO 12405-1. This time signal was then integrated twice and filtered to obtain a shaker test displacement imposed motion.

The results presented in section 6.2 show that there is indeed a global deformation in the battery observed in the full-vehicle simulations. This conclusion is taken from the fact that the global torsion and bending modes show the highest RMS MPF values overall.

The dynamic analysis of the shaker simulation shows a very low overall mode participation ($\sim 10^{-10}$), which is a result of the high level of constraint characteristic of the battery shaker simulation.

The MPF time histories from the full-vehicle simulations and shaker simulation had to be replicated so that compatibility between simulations was achieved. All the load cases were replicated to become representative of 100 000 miles of vehicle usage. Therefore, the pseudo-damage calculations were done for the same amount of vehicle usage and, as a result, can be compared.

The pseudo-damage is between 4.16 and 80.12 times higher in the full-vehicle simulations than in the battery simulations. For the full-vehicle simulations, the repeatability of each road seems to be the factor that mostly influences the damage. Roads that generate a higher modal participation (Pothole and D-class road) generate a slightly lower damage due to the fact that they are repeated less times in the 100 000 mile track. On the other side, the washboard out-of-phase road is the one with the largest amount if repetitions, and that generally gives the largest damage contribution for the vehicle simulations.

Overall, these results allow one to conclude that the shaker test is not appropriate for HV-battery durability testing, because it underestimates the damage that the battery suffers. To determine the loading that the HV-battery undergoes in a real-life scenario, full-vehicle simulations must be used instead.

7.2   Future Work

The limitations and future applications of the present project are hereby discussed.

- **Beams model**: The panels were disregarded in this model. This penalizes both the stiffness and mass of the truss structure. It is believed that integrating the panels in the beams model in order to create a hybrid structure could lead to slightly different modal properties. Namely, the structure would become more prone to local deformations in the panels and, as a result, the vibration frequencies would decrease.

- **Battery model**: The battery model used in this project has a level of detail that can be used to capture, mainly, global deformations in the battery pack. To represent correctly the local deformations in the battery pack, the battery finite element model would need a higher degree of detail.

- **MAC correlation (Members model vs. Truss model)**: Despite of the good correlation in the first 3 modes, it could be improved if the side panels of the car were accounted for in the members model. Additionally, the nodes that take part in the MAC correlation were manually selected. A scripted selection of nodes (for instance, via a MatLab program) could be used in order to associate nodes with the most similar coordinates. This association procedure could lead to better results in the MAC correlation.

- **Battery shaker simulation**: BEV HV-Battery vibration testing is a continuously developing topic, meaning that the standards defining the procedures for these tests are constantly updated and, in particular, the PSD profile suffers changes. This thesis focuses in one specific PSD vibration test standard that is commonly known in the industry. An evaluation of other standards could have been done, considering mainly more recent standards. Additionally, the SAE J2380 standard could have been also used in the battery shaker simulations. This comparison would have been done in terms of vertical acceleration comparison. Finally, the longitudinal components of all standard shaker vibration tests were neglected. It would be interesting to consider these longitudinal vibration excitations in one test at least to understand if they can actually be neglected.

- **Time signal derivation from PSD profile**: A self-developed script was created to calculate the acceleration time signal from the PSD profile to be applied to the battery in the shaker simulation. The imposed displacement was calculated in another self-developed script and subjected to filtering. The functionalities available in the Vibration data toolbox [53] also allow an automated determination of the displacement time-signal from an acceleration PSD profile. For early-stage validation, a displacement-level comparison between both signals could have been done.

- **Full-vehicle simulations**: The proving grounds used by OEM's for vehicle vibration testing purposes contain a large variety of road profiles. In this dissertation, a broader range of these profiles could have been use to improve the life-representative loading of the vehicle in the simulations. In particular, non-straight line events could have been studied, such as the double-lane-change, continuous radius curve and others.

  Additionally, the time-step chosen for the full-vehicle dynamic simulation does not allow the capture of high frequencies participating in the acceleration time signals. For future occasions, this time-step should be chosen according to the Nyquist-Shannon Sampling Theorem [49].

- **Modal Participation Factors**: Comparing the RMS value of the MPF's of the considered modes is useful to identify the most participating modes in the simulation. However, to determine the actual deformed shape of the structure under consideration (resultant from the linear combination of modes), a time-domain evaluation of each MPF is needed.

- **Pseudo-damage**: The pseudo-damage is only valid in relative terms between two comparable time-signals. In this project, the pseudo-damage concept was applied to the vertical acceleration time signal, resorting to a rainflow counting method to evaluate the severitiy of each load. However, this only allows a comparative analysis of the damage generated in each loading and not an effective calculation of the real damage. To tackle this issue, a fatigue analysis could have been done. The fatigue analysis accounts with the properties of the materials considered (Yield strength, Ultimate tensile strength, Miner rule curve, Haigh diagram, etc..) [54], analysis-specific paramters (probaility of survival, critical nodes, etc..) and a time-history of the modal participation factors to calculate the damage and life of a certain component. FemFat is a commercial simulation software that could have been used for this purpose.

Bibliography

[1] CO_2 emissions from cars: facts and figures (infographics). `https://www.europarl.europa.eu/news/en/headlines/society/20190313STO31218/co2-emissions-from-cars-facts-and-figures-infographics`, . Accessed: 2021-03-22.

[2] 2030 climate energy framework. `https://ec.europa.eu/clima/policies/strategies/2030_en`, . Accessed: 2021-03-22.

[3] Explainer: Why automakers are on a drive to sell electric cars in europe. `https://www.reuters.com/article/us-autoshow-geneva-carbon-explainer-idUKKBN20Q1MM`. Accessed: 2021-03-22.

[4] Internal-combustion vehicle bans across the world. `https://www.autoblog.com/2020/11/18/internal-combustion-engine-bans-around-the-world/?guccounter=1&guce_referrer=aHR0cHM6Ly93d3cuZ29vZ2xlLmNvbS88&guce_referrer_sig=AQAAAGiseTmdvAbfFEYkzlMfNskpB-1lxVOnMoF_LkEuI4lWwO_4NW_8KL_x_vbsOtTOrfrS6cQ_4loOYTN7sKF_EuGX5VRhvGEZBvDakOJQuYOX1j1eXZglktE86gQjPohSF2RWOBkGXwMadUkfJsGWmPRmCaSMxWegWMeowo_6A-8i`. Accessed: 2021-03-22.

[5] McKinsey Report. Electromobility's impact on powertrain machinery, may 2021. `https://www.mckinsey.com/industries/automotive-and-assembly/our-insights/electromobilitys-impact-on-powertrain-machinery` Accessed: 2021-10-27.

[6] A. Dörnhöfer. *Betriebsfestigkeitsanalyse elektrifzierter Fahrzeuge*. Springer, 2018.

[7] P. Johannesson, M. Speckert. *Guide to Load Analysis for Durability in Vehicle Engineering*. Wiley, 2014.

[8] A. Rissoan. Damage and equivalent load definition for mechanical durability of subframe. Master's thesis, ENSTA Bretagne, 2018.

[9] International Electrotechnical Comission Standard 60068-2-64:2008. Environmental testing - Part 2-64: Tests - Test Fh: Vibration, broadband random and guidance.

[10] N. Maia, J. M. e Silva. *Vibrações e ruído.* AEIST, 1996.

[11] J. P. Bianchi, E. Balmès, G. Vermot Des Roches, and A. Bobillot. Using modal damping for full model transient analysis. Application to pantograph/catenary vibration. In *ISMA*, page 376, Leuven, Belgium, Sept. 2010. URL `https://hal.archives-ouvertes.fr/hal-00589953`.

[12] J. T. Katsikadelis. *Dynamics of Structures*. Matthew Deans, 2020.

[13] *NX Nastran - Basic Dynamic Analysis User's Guide*. MSC Software, 2009.

[14] *Nastran Superelement user's guide*. MSC Software, 2001.

[15] E. G. Al-Hasany, A. H. Alsalmani, S. R. Al-Zaidee. Effectiveness of connections type on vibration response of steel beam. *Civil Engineering Journal*, 2019.

[16] J. M. Hooper, J. Marco, G. H. Chouchelamane, J. S. Chevalier, D. Williams. Multi-axis vibration durability testing of lithium ion 18650 nca cylindrical cells. *Journal of Energy Storage*, 2017.

[17] Crystal Instruments. Basics of Modal Testing and Analysis, 2016. `https://www.crystalinstruments.com/basics-of-modal-testing-and-analysis` Accessed: 2021-10-27.

[18] Data Physics. FRF (Frequency Response Function) Measurement, . `https://www.dataphysics.com/applications/structural-testing/frf-frequency-response-function-measurement.html` Accessed: 2021-10-27.

[19] B. J. Schwarz, Mark H. Richardson. Experimental modal analysis. *CSI Reliability Week*, 1999. `https://www.maintenance.org/fileSendAction/fcType/0/fcOid/399590942963653618/filePointer/399590942964787702/fodoid/399590942964787700/28-_Experimental_Modal_Analysis.pdf` Acessed:2021-10-27.

[20] Data Physics. Data Physics EV battery vibration testing systems, . `https://www.youtube.com/watch?v=vMWUpLiq1eI` Accessed: 2021-11-02.

[21] Sentek Dynamics. Sentek Dynamics' Turn-key Solutions for Battery Testing in a Combined Environment, 2021. `https://www.wikiwand.com/en/Friction_stir_spot_welding` Accessed: 2021-10-30.

[22] ISO 12405-1. Electrically propelled road vehicles — Test specification for lithium-ion traction battery packs and systems . Standard, International Organization for Standardization, Geneva, CH, Mar. 2011.

[23] ISO 6469-1. Electrically propelled road vehicles — Safety specifications - Rechargeable energy storage system (RESS) . Standard, International Organization for Standardization, Geneva, CH, Mar. 2019.

[24] S. Hanly. Vibration Analysis: FFT, PSD, and Spectrogram Basics. `https://blog.endaq.com/vibration-analysis-fft-psd-and-spectrogram` Accessed: 2021-10-27.

[25] National Instruments. Understanding FFTs and Windowing . `https://pdf4pro.com/view/understanding-ffts-and-windowing-22e984.html` Accessed: 2021-10-27.

[26] K. Shin, J. Hammond. *Signal Processing for Sound and Vibrations Engineers*. Wiley, 2008.

[27] Vibration Research. Calculation PSD From a Time History File, 2019. `https://vru.vibrationresearch.com/lesson/calculating-psd-time-history/` Accessed: 2021-10-28.

[28] Society of Automotive Engineers Standard J2380, 2013. Vibration Testing of Electric Batteries.

[29] J. M. Hooper, J. Marco . Defining a Representative Vibration Durability Test for Electric Vehicle (EV) Rechargeable Energy Storage Systems (RESS). *World Electric Vehicle Journal*, 2016.

[30] D. G. M. J. G. Proakis. *Digital Signal Processing. Principles, Algorithms and Applications*. Wiley, 2007.

[31] P. Johannesson and M. Speckert. *Guide to Load Analysis for Durability in Vehicle Engineering*. Wiley, 2014.

[32] Y.-L. Lee and T. Tjhung. Rainflow cycle counting techniques. pages 89–114. Elsevier, 2012. doi: 10.1016/b978-0-12-385204-5.00003-3. URL `https://doi.org/10.1016/b978-0-12-385204-5.00003-3`.

[33] I. Ed-Dokkali, L. E. Bakkali. Stress Distribution Dynamic Study Due to the Bending Mode of the Wind Turbine Blade. *International Journal of Mechanics and Applications*, 2016.

[34] B. D. Lévai. Damage and equivalent load definition for durability of vehicle. Master's thesis, Linköping University, 2018.

[35] S. S. Prakash. A method of accelerating durability tests by pseudo damage editing. SAE International, Jan. 2013. doi: 10.4271/2013-26-0138. URL `https://doi.org/10.4271/2013-26-0138`.

[36] C. M. Stewart,. Stress-Life Approach. Lecture Notes, 2021. `http://me.utep.edu/cmstewart/documents/ME5390Fatigue/Lecture%204%20-%20Stress-Life%20Approach.pdf`.

[37] Autoprova. Focus on the high-voltage battery system of the Audi e-tron: 95 kWh of energy, 2019. `https://autoprova.be/2019/04/01/focus-on-the-high-voltage-battery-system-of-the-audi-e-tron-95-kwh-of-energy/` Accessed:2021-10-28.

[38] A2Mac1. Audi e-tron 55 Quattro Edition One 2019, 2019. `https://portal.a2mac1.com/`Accessed: 2021-11-1.

[39] G. De Gaetano, D. Mundo, C. Maletta, M. Kroiss, L. Cremers. Multi-objective optimization of a vehicle body by combining gradient-based methods and vehicle concept modelling. *Elsevier*, 2015.

[40] C. Gui, W. Zuo. Simplified and fast modeling of automotive body frame. *The 8th International Conference on Computational Methods*, 2017.

[41] BETA CAE Systems. New Beam Modeling through EPILYSIS. `https://www.youtube.com/watch?v=hr9UVOgtBi4` Accessed: 2021-10-27.

[42] Wikiwand. Friction stir spot welding. `https://www.wikiwand.com/en/Friction_stir_spot_welding` Accessed: 2021-10-28.

[43] *Adams Release Guide*. MSC Software, 2005.

[44] International Standard ISO 8608:2016 Mechanical vibration — Road surface profiles — Reporting of measured data. Electrically propelled road vehicles — Test specification for lithium-ion traction battery packs and systems.

[45] D. Y. M. Reddy, S. Padmanabhan. Virtual full vehicle durability testing of a passenger car. Master's thesis, Chalmers University of Technology, 2017.

[46] L. Liu. Evaluation of the feasibility of posting reduced speed limits on kansas gravel roads. 11 2021.

[47] Transportation Reaserch Center Inc. Virtual Facility Tour, 2020. `https://www.trcpg.com/virtual-facility-tour/` Accessed: 2021-11-02.

[48] A. Dinis. Influence of suspension parameters on vehicle durability. Master's thesis, Instituto Superior Técnico, Universidade de Lisboa, 2018.

[49] S. BenZvi. Physics 403 - Spectral Analysis. `https://www.pas.rochester.edu/~sybenzvi/courses/phy403/2015s/p403_21_spectral_analysis.pdf` Accessed: 2021-11-02.

[50] J. M. Hooper, J. Marco . Characterising the in-vehicle vibration inputs to the high voltage battery of an electric vehicle. *Journal of Power Sources*, 2014.

[51] Automotive Testing Technology International. AVL ZalaZONE Proving Ground Ltd. `https://www.automotivetestingtechnologyinternational.com/supplier-spotlight/avl-zalazone-proving-ground-ltd` Accessed: 2021-11-02.

[52] Math. Stat., Center for Math. Sci., Lund Univ. WAFO - Main features. `https://www.maths.lth.se/matstat/wafo/` Accessed: 2021-11-02.

[53] T. Irvine. *An Introduction to Shock and Vibration Spectra*. Endaq, 2020.

[54] *Manual FEMFAT 5.4*. Magna, 2019.